



NAVAL POSTGRADUATE SCHOOL

MONTEREY, CALIFORNIA

THESIS

**LANGMUIR PROBE DIAGNOSTICS OF THE VASIMR
ENGINE**

by

Brian Collins Sinclair

December 2005

Thesis Advisor:
Second Reader:

Chirolde Epp
Christopher Brophy

Approved for public release; distribution is unlimited

THIS PAGE INTENTIONALLY LEFT BLANK

REPORT DOCUMENTATION PAGE			<i>Form Approved OMB No. 0704-0188</i>	
Public reporting burden for this collection of information is estimated to average 1 hour per response, including the time for reviewing instruction, searching existing data sources, gathering and maintaining the data needed, and completing and reviewing the collection of information. Send comments regarding this burden estimate or any other aspect of this collection of information, including suggestions for reducing this burden, to Washington headquarters Services, Directorate for Information Operations and Reports, 1215 Jefferson Davis Highway, Suite 1204, Arlington, VA 22202-4302, and to the Office of Management and Budget, Paperwork Reduction Project (0704-0188) Washington DC 20503.				
1. AGENCY USE ONLY (Leave blank)		2. REPORT DATE December 2005	3. REPORT TYPE AND DATES COVERED Master's Thesis	
4. TITLE AND SUBTITLE: Langmuir Probe Diagnostics of the VASIMR Engine			5. FUNDING NUMBERS	
6. AUTHOR(S) Brian Collins Sinclair				
7. PERFORMING ORGANIZATION NAME(S) AND ADDRESS(ES) Naval Postgraduate School Monterey, CA 93943-5000			8. PERFORMING ORGANIZATION REPORT NUMBER	
9. SPONSORING /MONITORING AGENCY NAME(S) AND ADDRESS(ES) N/A			10. SPONSORING/MONITORING AGENCY REPORT NUMBER	
11. SUPPLEMENTARY NOTES The views expressed in this thesis are those of the author and do not reflect the official policy or position of the Department of Defense or the U.S. Government.				
12a. DISTRIBUTION / AVAILABILITY STATEMENT Approved for public release; distribution is unlimited			12b. DISTRIBUTION CODE	
13. ABSTRACT (maximum 200 words) NASA's VArIable Specific Impulse Magnetoplasma Rocket Engine (VASIMR) will provide a highly efficient propulsion source that can dramatically reduce Martian transit times, provide for more abort contingencies, and protect astronauts from space radiation with its highly radiation-absorbent hydrogen fuel. The VASIMR is still in its developmental infancy and requires many years of research before its initial operational capability. Much is still unknown about the complex plasma interactions in the exhaust. A Langmuir probe was designed, constructed, and operated to determine current density radial profiles and total particle flux at various stages in the exhaust of VASIMR. The Langmuir probe results proved that the exhaust's radial profile is Gaussian, experimentally validated predictions of magnetic field line dragging, and verified the ionization efficiency of VASIMR.				
14. SUBJECT TERMS Langmuir Probe Diagnostics, Plasma Physics, VASIMR Engine, Magnetoplasma Rocket Engine, Electric Propulsion, Ion Engine			15. NUMBER OF PAGES 107	
			16. PRICE CODE	
17. SECURITY CLASSIFICATION OF REPORT Unclassified	18. SECURITY CLASSIFICATION OF THIS PAGE Unclassified	19. SECURITY CLASSIFICATION OF ABSTRACT Unclassified	20. LIMITATION OF ABSTRACT UL	

NSN 7540-01-280-5500

Standard Form 298 (Rev. 2-89)
Prescribed by ANSI Std. Z39-18

THIS PAGE INTENTIONALLY LEFT BLANK

Approved for public release; distribution is unlimited

LANGMUIR PROBE DIAGNOSTICS OF THE VASIMR ENGINE

Brian C. Sinclair
Lieutenant, United States Navy
Aerospace Engineering B.S., U.S. Naval Academy, 1997

Submitted in partial fulfillment of the
requirements for the degree of

MASTER OF SCIENCE IN ASTRONAUTICAL ENGINEERING

from the

**NAVAL POSTGRADUATE SCHOOL
December 2005**

Author: Brian C. Sinclair

Approved by: Dr. Chiold Epp
Thesis Advisor

Dr. Christopher Brophy
Second Reader

Dr. Anthony J. Healey
Chairman, Department of Mechanical and Astronautical
Engineering

THIS PAGE INTENTIONALLY LEFT BLANK

ABSTRACT

NASA's VArIable Specific Impulse Magnetoplasma Rocket Engine (VASIMR) will provide a highly efficient propulsion source that can dramatically reduce Martian transit times, provide for more abort contingencies, and protect astronauts from space radiation with its highly radiation-absorbent hydrogen fuel. The VASIMR is still in its developmental infancy and requires many years of research before its initial operational capability. Much is still unknown about the complex plasma interactions in the exhaust. A Langmuir probe was designed, constructed, and operated to determine current density radial profiles and total particle flux at various stages in the exhaust of VASIMR. The Langmuir probe results proved that the exhaust's radial profile is Gaussian, experimentally validated predictions of magnetic field line dragging, and verified the ionization efficiency of VASIMR.

THIS PAGE INTENTIONALLY LEFT BLANK

TABLE OF CONTENTS

I.	INTRODUCTION.....	1
A.	BACKGROUND	1
B.	PLASMA PROPULSION PHYSICS	1
	1. Plasma Properties	1
	<i>a. Quasi-Neutrality.....</i>	<i>1</i>
	<i>b. Collective Behavior</i>	<i>3</i>
	<i>c. Temperature</i>	<i>3</i>
	<i>d. Plasma Interactions in a Magnetic Field.....</i>	<i>6</i>
	2. VASIMR Engine	8
	<i>a. History</i>	<i>8</i>
	<i>b. Operation Basics</i>	<i>9</i>
	<i>c. Advantages</i>	<i>9</i>
	<i>d. Experimental Configuration.....</i>	<i>11</i>
	<i>e. Field Line Dragging Experiment</i>	<i>13</i>
II.	LANGMUIR PROBE	17
A.	BACKGROUND	17
	1. History.....	17
	2. Theories Evolve	17
	3. Orbital Motion-Limited Theory	18
	4. Operation	19
B.	CONSTRUCTION.....	22
	1. Location and Size	22
	2. Material Selection	24
	3. Manufacture and Assembly	27
	4. Pre-Amplifier Construction	32
	<i>a. Isolation Amplifier</i>	<i>32</i>
	<i>b. Sensing Resistors</i>	<i>35</i>
	<i>c. LC Filter</i>	<i>36</i>
	5. Calibration.....	38
III.	RESULTS/ANALYSIS	41
A.	RAW DATA	41
B.	ANALYSIS ALGORITHMS	41
	1. Noise Filter.....	42
	2. Current Density Calculations	46
	3. Current Density Radial Profile.....	53
	4. Flux Calculations	59
	5. Ionization Efficiency	65
	6. Field Line Dragging Experimental Results	66
IV.	CONCLUSIONS	69

A.	RADIAL PROFILE VERIFICATION	69
B.	FIELD LINE DRAGGING EXPERIMENT	69
C.	FLUX AND IONIZATION EFFICIENCY	69
APPENDIX A.	A PROPOSED DEMONSTRATION OF FIELD-LINE DRAGGING IN VASIMR	71
APPENDIX B.	MATLAB TEMPORAL CURRENT DENSITY PROGRAM.....	77
APPENDIX C.	MATLAB RADIAL PROFILE PROGRAM.....	81
APPENDIX D.	MATLAB FLUX DETERMINING PROGRAM.....	87
APPENDIX E.	MATLAB GAS FLOW PROGRAM	89
INITIAL DISTRIBUTION LIST	91

LIST OF FIGURES

Figure 1.	Debye Shielding.....	2
Figure 2.	Maxwellian Velocity Distribution	4
Figure 3.	Magnetic Mirroring Between Two Ring Magnets.....	8
Figure 4.	DRM 3 Timeline	10
Figure 5.	VASIMR Proposed Launch Profile	11
Figure 6.	VX-10 Configuration.....	12
Figure 7.	Normal Magnetic Field Lines	14
Figure 8.	Weak Field Lines	15
Figure 9.	Plasma Dragging Lines into Weak Region.....	15
Figure 10.	Reverse Polarity Coil Current.....	16
Figure 11.	Characteristic Curve.....	19
Figure 12.	Collector Plate Orientation	21
Figure 13.	Experimental Set Up	22
Figure 14.	Diagram of Probe Placement	23
Figure 15.	Gate Valves Used to Insert Probe	23
Figure 16.	Tungsten Collector Plate With Ceramic Collar	26
Figure 17.	Actual Probe Discs With Macor	27
Figure 18.	Collar and Disc Dimensions	28
Figure 19.	Disc and Collar Mating.....	29
Figure 20.	Collector Orientation	29
Figure 21.	Feedthrough and Signal Wires.....	30
Figure 22.	Complete Feedthrough with Cannon Plug.....	31
Figure 23.	Model of Total Probe Construction	31
Figure 24.	Complete Probe Construction.....	32
Figure 25.	Block Diagram of AD215.....	33
Figure 26.	Prototype Pre-Amplifier Schematic.....	33
Figure 27.	ISO124 Wiring Diagram.....	34
Figure 28.	ISO124 Performance Curve.....	35
Figure 29.	Pre-Amplifier Schematic	37
Figure 30.	10 Circuit Pre-Amp Box	38
Figure 31.	Noisy Raw Data from Collector#1	41
Figure 32.	Direct Form II Transposed Filter	42
Figure 33.	DF2T Filtered Signal	43
Figure 34.	Filters With Various Cut-Off Frequencies.....	44
Figure 35.	Filters With Various Orders.....	45
Figure 36.	External Distance Measure	46
Figure 37.	Port #1 Current Density Vs Time (shot 44)	47
Figure 38.	Position With Respect to Plasma Centerline (shot 44)	47
Figure 39.	Position With Respect to Plasma Centerline (shot 32)	48
Figure 40.	Port #1 Current Density Vs Time (shot 32)	49
Figure 41.	Port #1 Current Density Vs Time (shot 45).....	50

Figure 42.	Position With Respect to Plasma Centerline (shot 45)	50
Figure 43.	Port #2 Current Density vs Time (shot 42)	51
Figure 44.	Port #2 Current Density Vs Time (shot 80)	52
Figure 45.	Probe Immersed in Plasma.....	53
Figure 46.	Port #1 Radial Profile (shot44)	55
Figure 47.	Port #1 Radial Profile (shot 32)	56
Figure 48.	Port #1 Radial Profile (shot 45)	57
Figure 49.	Port #2 Radial Profile (shot 42)	58
Figure 50.	Port #2 Radial Profile (shot 80)	59
Figure 51.	Annular Current Formula Calculation	60
Figure 52.	Port #1 Flux and Error Calculations (shot 44)	61
Figure 53.	Port #1 Flux and Error Calculations (shot 32)	62
Figure 54.	Port #1 Flux and Error Calculations (shot 45)	63
Figure 55.	Port #2 Flux and Error Calculations (shot 42)	64
Figure 56.	Port #2 Flux and Error Calculations (shot 33)	65
Figure 57.	Standard VASIMR Gas Flow for Deuterium.....	66
Figure 58.	Radial Profiles with Varying Coil Currents.....	67

LIST OF TABLES

Table 1.	Port Characteristics	24
Table 2.	Element Properties,,	25
Table 3.	Resistance Values and Resulting Signal Voltages.....	36
Table 4.	Sensing Resistor Values.....	36
Table 5.	LC Filter Values.....	37
Table 6.	Percent Error For Shots 42 and 80.....	59

THIS PAGE INTENTIONALLY LEFT BLANK

ACKNOWLEDGMENTS

I would like to thank Drs. Chiold Epp, Franklin Chang Diaz, and Tim Glover for their support throughout my work. I would also like to thank Mr. Sam Barone for his help and my lovely wife for her patience throughout this whole process.

THIS PAGE INTENTIONALLY LEFT BLANK

I. INTRODUCTION

A. BACKGROUND

For years, man has dreamt of traveling the solar system. Recently the successes of the Martian rovers, Opportunity and Spirit, and President Bush's "Mars Initiative" are revitalizing those dreams. Many technological advances are needed before man can safely and efficiently travel to the red planet. The chemical engines of today are not the optimal solution for manned interplanetary travel for several reasons. Use of chemical engines is inefficient and requires large amounts of propellant mass. The "fire and drift" fuel scheduling of chemical engines generally requires long drift times. These long drift times equate to longer crew exposure time to hostile space radiation and microgravity environments while limited fuel supply minimizes mission-abort contingencies. Greater efficiency, speed, and abort opportunities can be afforded by continuous-thrust electric propulsion engines. The higher exhaust velocities of electric propulsion create much higher steady state specific impulse (300-3000 sec) from that of bipropellant engines (313-322 sec)¹. The ten-fold increase in specific impulse leads to much greater fuel efficiency.

B. PLASMA PROPULSION PHYSICS

1. Plasma Properties

In the late 1920s, Dr. Irving Langmuir was studying the unusual magnetic and electric characteristics of super-heated gases. He coined the term "plasma" to describe the soup of ionized particles because their nature reminded him of the way blood plasma carries its constituents. A more useful definition of plasma is "a quasi-neutral gas of charged and neutral particles which exhibits collective behavior".²

a. Quasi-Neutrality

The quasi-neutrality of plasma is based on the fact that electron and ion densities are relatively equal and are called the common or plasma density. The plasma,

¹ Larson, Wiley J. and James R. Wertz, Space Mission Analysis and Design, Third Edition, (Microcosm Press, El Segundo, CA) 688.

² Chen, Francis F. *Introduction to Plasma Physics and Controlled Fusion*, Second Edition, (Plenum Press, New York) 3.

however, is not neutral and retains all of its peculiar electromagnetic traits. One of those traits is its ability to shield applied electric fields. If one were to place two oppositely charged objects in a plasma, each object would attract oppositely charged plasma constituents. The clouds of particles or sheaths around each object, as depicted in Figure 1, exactly counter the charge contained within, thus preventing an electric field from forming within the plasma.

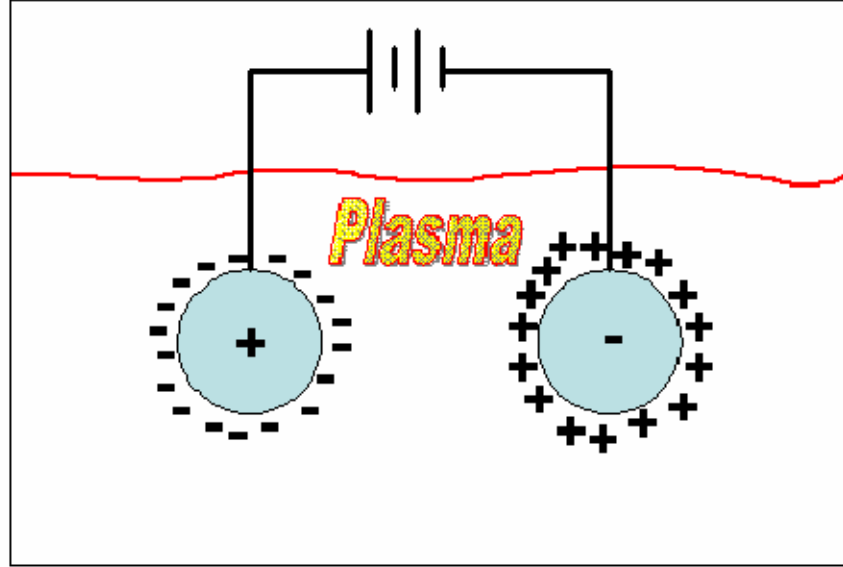


Figure 1. Debye Shielding

The thickness of such clouds is called the Debye length, λ , where

$$\lambda_D = \left(\frac{\epsilon_0 K T_e}{n e^2} \right)^{\frac{1}{2}}$$

and ϵ_0 is free space permittivity, K is Boltzmann's constant, T_e is electron temperature in Kelvin, n is electron density, and e is electron charge. A formal derivation of Debye length can be found in *Introduction to Plasma Physics and Controlled Fusion, Second Edition* by Francis F. Chen pages 8-10. The expression for Debye length can be further simplified into a more useful form by inserting the constants and converting lengths from meters to centimeters

$$\lambda_D = 743 \left(\frac{KT_e}{n} \right)^{\frac{1}{2}}$$

where KT_e is measured in eV and n (density) is cm^{-3} . This calculation will be used when determining probe size.

b. Collective Behavior

In a neutral gas, molecules affect each other only through collisions. This is not the case in a plasma consisting of neutral and charged particles. The charged particles exert Coulombic forces on each other and can produce local regions of charge concentration. These moving regions produce electric fields and current-induced magnetic fields. These fields can affect motions of other long-distance, charged regions. Regional interactions can be so strong, that many assume plasmas to be collisionless³. This common simplification asserts that the electromagnetic interactions are much stronger than individual particle collisions so the latter can be neglected. These interactions can cause a plasma to react erratically to an external force thus seeming to have a mind of its own.

c. Temperature

A gas in thermal equilibrium will contain particles with a Maxwellian distribution of velocities. For simplicity, one can assume that the plasma will consist of particles that only move in one direction⁴. The one-dimensional Maxwellian distribution is given by

$$f(v) = Ae^{\frac{-mv^2}{KT}}$$

where $f(v)$ is the number of particles per cubic meter with a speed between v and $v + dv$, $\frac{1}{2}mv^2$ is the kinetic energy, and the constant A is related to density (n),

³ Chen, Francis F. *Introduction to Plasma Physics and Controlled, Fusion* Second Edition,(Plenum Press, New York) 4.

⁴ Chen, Francis F. *Introduction to Plasma Physics and Controlled, Fusion* Second Edition,(Plenum Press, New York) 5.

$$n = \int_{-\infty}^{\infty} f(u) du$$

by

$$A = n \left(\frac{m}{2\pi KT} \right)^{\frac{1}{2}}$$

The width of the distribution is characterized by the temperature, T. Figure 2 depicts a typical Maxwellian distribution for particle density ($f(u)$) with a varying velocities.

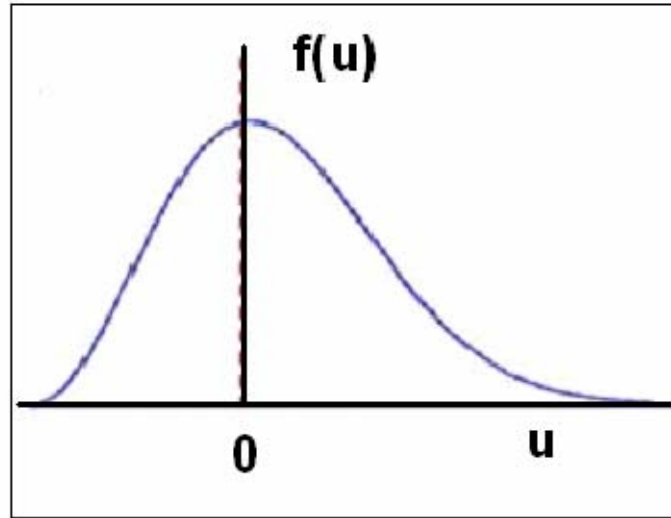


Figure 2. Maxwellian Velocity Distribution

The average kinetic energy can be determined from

$$E_{av} = \frac{\int_{-\infty}^{\infty} \frac{1}{2} m v^2 f(v) dv}{\int_{-\infty}^{\infty} f(v) dv}$$

and defining the relation

$$\frac{1}{2} m v^2 = KT$$

where $K = 1.38 \times 10^{-23} \text{ J/K}$ (Boltzmann's Constant) After some tedious integration and substitution, it can be shown that

$$E_{av} = \frac{\frac{1}{4} m A v^3}{A v} = \frac{1}{4} m v^2 = \frac{1}{2} K T$$

If the Maxwellian distribution is extended to three dimensions with triple integrals, the complex expression can be reduced to show

$$E_{av} = \frac{3}{2} K T$$

Average kinetic energy and temperature are so closely related that plasma temperature is often displayed in units of energy. To eliminate dimensional ambiguity, physicists usually refer to energy corresponding to $K T$ when discussing plasma temperature⁵.

$$K T = 1 e V = 1.6 \times 10^{-19} \text{ J}$$

or by rearranging

$$T = \frac{1.6 \times 10^{-19} \text{ J}}{1.38 \times 10^{-23} \text{ J / K}} = 11600 \text{ K}$$

thus the conversion factor is

$$1 e V = 11,600^\circ \text{ K}$$

The ions and electrons in a plasma can have separate Maxwellian distributions and temperatures. This is mainly due to the same species collision rates being higher than ion-electron collision rates. Each constituent can have a different energy level and thermal equilibrium with a difference of an order of magnitude. Sometimes the plasma does not last long enough for the two temperatures to equalize. The VASIMR engine deals with imparting energy to the heavier ions ($m_{ion} = 1836 m_{e-}$),

⁵ Chen, Francis F. *Introduction to Plasma Physics and Controlled Fusion*, Second Edition, (Plenum Press, New York) 7.

because of the much larger momentum transfer when they exit the rocket chamber. For reference, the working plasma will have an electron temperature of approximately 7 eV⁶.

d. Plasma Interactions in a Magnetic Field

The moving charged particles in the VASIMR engine are exposed to varying magnetic fields. These particles experience a force

$$\vec{F} = q\vec{v} \times \vec{B}$$

where q is the particle charge, v is the velocity, and B is the magnetic field. From the definition of cross product, the force is perpendicular to both the velocity and magnetic field lines. This creates a gyrating motion about the magnetic field lines. The radius of gyration or L'Armor radius is easily found by substituting angular acceleration, $\frac{v^2}{r}$, into the above equation and solving for r:

$$r = \frac{mv}{|q|B}$$

Knowing from basic kinetics that tangential velocity is related to angular velocity by

$$\omega r = v$$

one can solve for the angular rate or gyration frequency of a particle given by:

$$\omega_c = \frac{|q|B}{m}$$

This frequency is commonly called the cyclotron frequency⁷. The cyclotron frequency is important when imparting energy to a specific species in much the same way a structure can be efficiently excited at its natural frequency. The VASIMR Ion Cyclotron Resonance Heating (ICRH) antenna transmits RF energy at the ion cyclotron frequency for efficient heating of ions.

⁶ Chang Diaz, F.R. et al, "Particle Simulations of Plasma Heating in VASIMR" AIAA-2000-3753, 2.

⁷ Chen, Francis F. *Introduction to Plasma Physics and Controlled Fusion*, Second Edition,(Plenum Press, New York) 20.

Meanwhile, the helicon antenna, responsible for plasma production, transmits RF near the lower hybrid frequency, ω_{LH} ,

$$\frac{1}{\omega_{LH}^2} = \frac{1}{\omega_{ce}\omega_{ci}} + \frac{1}{\omega_{pi}^2} + \frac{1}{\omega_{ci}^2}$$

where ω_{ce} is the electron cyclotron frequency, ω_{ci} is the ion cyclotron frequency, and ω_{pi} is the ion plasma frequency. These three frequencies are found by inserting the respective particle masses into the previously mentioned gyration frequency equation. The lower hybrid frequency is a good balance between species' cyclotron frequencies to produce efficient ionization. A more formal derivation of the lower hybrid frequency can be found in *Plasma Physics and Controlled Fusion, Second Edition* by Francis F. Chen pages 112-113.

The gyrating particle has a magnetic moment defined as

$$\mu = \frac{\frac{1}{2}mv_{\perp}^2}{B}$$

where v_{\perp} is the velocity component perpendicular to the magnetic field line. The magnetic moment (μ) is invariant. The total energy (parallel and perpendicular velocity components) of the particle is also conserved. Thus, as the local magnetic field increases, v_{\perp} must also increase to maintain μ . This means that v_{\parallel} will decrease to conserve energy. This phenomenon is known as magnetic mirroring and is a typical plasma containment method. VASIMR uses this concept with its “magnetic beach” containment⁸. This method contains the ions in the ICRH section until they have been imparted with sufficient energy to be expanded through the magnetic nozzle and produce thrust.

⁸ Chang Diaz, F.R. et al., “The Physics and Engineering of the VASIMR Engine,” AIAA-2000-3756, 4.

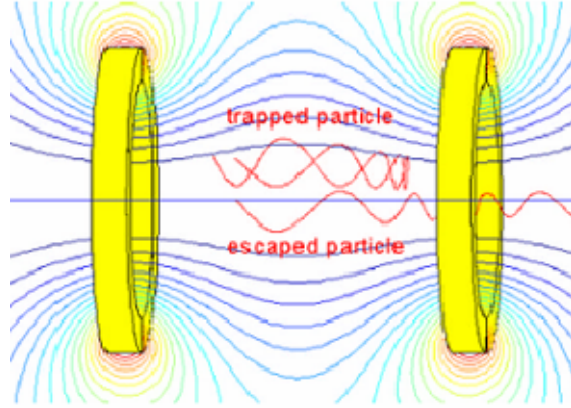


Figure 3. Magnetic Mirroring Between Two Ring Magnets

A magnetically confined plasma has a parameter, β , which indicates its kinetic energy with respect to the magnetic field energy density. This parameter quantifies how influential the magnetic fields are to a plasma.

A lower β indicates a strong magnetic field.

$$\beta = \frac{nKT}{\left(\frac{B^2}{2\mu_o}\right)}$$

where nKT is the plasma pressure and $\frac{B^2}{2\mu_o}$ is the magnetic field pressure. Inside the VASIMR engine, the magnetic field dominates the plasma and $\beta < 1$, however the diverging magnetic field lines in the aft portion of the engine allow β to approach unity.

2. VASIMR Engine

a. History

NASA's Advanced Space Propulsion Laboratory (ASPL) in Houston, Texas is continuing the development of an engine, called the Variable Specific Impulse Magnetoplasma Rocket engine, or VASIMR. The design concept for VASIMR dates back to the late 1970s when the Charles Stark Draper Lab at the Massachusetts Institute

of Technology was studying open-ended fusion devices⁹. In the early 1980s, the experiment gained more momentum as NASA and the USAF Office of Scientific Research began funding the program. In 1993, the ever-growing experiment was relocated to Johnson Space Center in Houston.

b. Operation Basics

VASIMR uses high-energy plasma to produce a continuously thrusting engine that can modulate exhaust velocity. This technique, called constant power throttling (CPT), distributes input power between the two major components of the engine, the ionizing helicon antenna and the ion cyclotron resonance heating antenna¹⁰. CPT is similar to the operation of an automobile transmission such that in strong gravity fields, more power is directed to ionization for thrust (low gear) while once away from a planet, the engine can shift power to increase specific impulse (high gear). Matching exhaust velocity to vehicle speed optimizes engine power output.

c. Advantages

In addition to efficiency, VASIMR offers access to a nearly limitless fuel supply. Currently, ASPL is conducting experiments using hydrogen, helium, and deuterium as fuels. Hydrogen is one of the most prevalent elements in the universe and is also a major by-product of space life support systems. Ideally, interplanetary ships could store the excess hydrogen in tanks surrounding crew stations so the fuel could double as protection against solar proton events and other radiation hazards. Greater fuel quantity will provide for more abort options during the heliocentric trajectory to Mars.

NASA's Design Reference Mission Version 3.0 (DRM 3) was published as a baseline for comparison of manned missions to Mars. In the study, three types of interplanetary trajectories are suggested, short-stay, long-stay, and fast transit. Figure 4 depicts the fast transit trajectory. Each transit's propulsion demands are inversely proportional to time required. The best-case scenario, fast transit, requires 150 days for trans-Martian injection and 110 days for the return trip. Abort opportunities are

⁹ Chang Diaz, F.R., "An Overview of the VASIMR Engine: High Power Space Propulsion with RF Plasma Generation and Heating", Invited Paper, American Institute of Physics 14th Topical Conference on RF Power in Plasmas, Oxnard, CA, May 2001, 1.

¹⁰ Chang Diaz, F.R. et al., "The Physics and Engineering of the VASIMR Engine," AIAA-2000-3756, 2.

extremely limited and once past halfway, require the crew to abort to a Martian orbit. From there, the crew must wait until the next Earth-Mars window of opportunity opens. Windows open every 2.2 years. A separate study was conducted using three 12kW VASIMR engines. Transits took 115 and 89 days to and from Mars, respectively (see Figure 5). Earth abort windows were available until the 80th day of the transit. Although the return trip could take as long as 1.25 years, it would not require the crew wait 2.2 years in a Martian orbit.

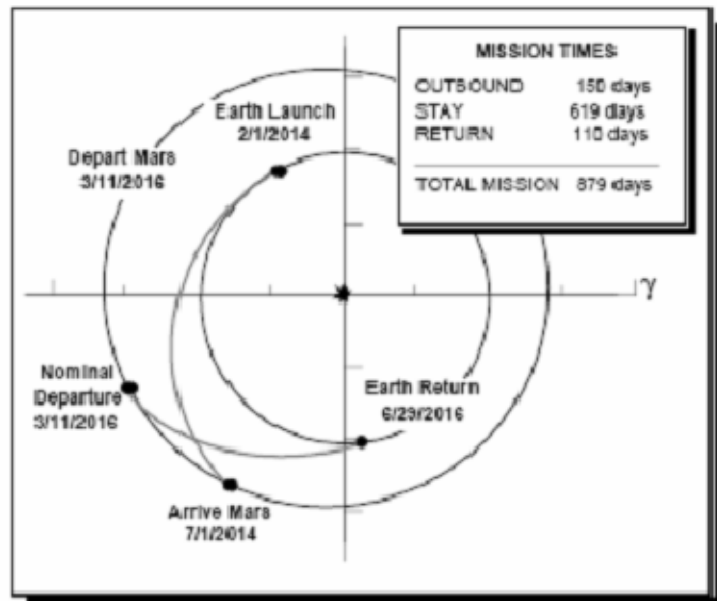


Figure 4. DRM 3 Timeline

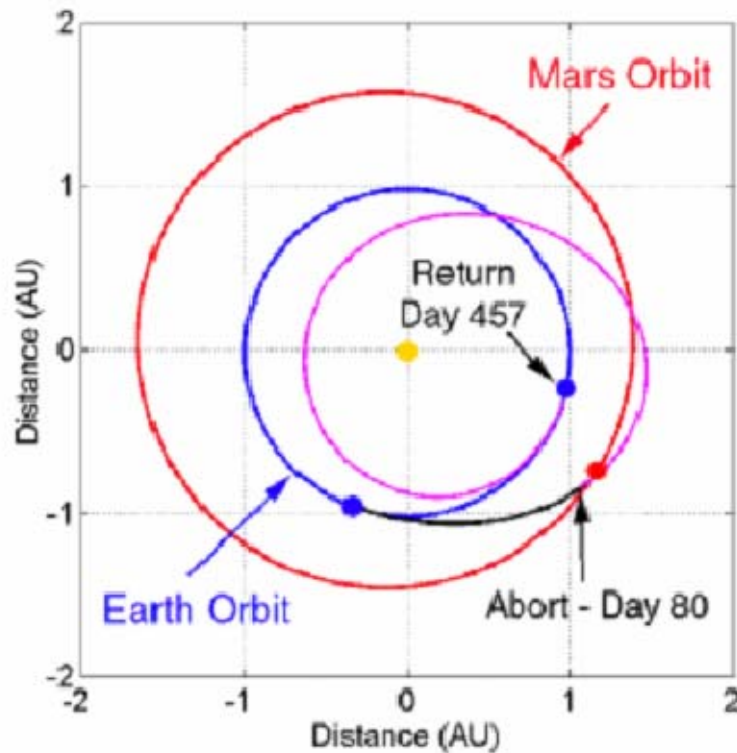


Figure 5. VASIMR Proposed Launch Profile¹¹

d. Experimental Configuration

The VASIMR experiment at ASPL, the VX-10, is a linear plasma containment device consisting of three chambers that use RF and magnetic mirror geometry to ionize, accelerate, and direct the plasma. Each chamber is created by axially varying magnetic fields. In the first chamber, the fuel is ionized using right-hand circularly polarized RF energy called helicon waves. The helicon antenna is isolated from the plasma by a quartz tube. This tube prevents ablation and eventual destruction of the antenna. The water-cooled, half-turn helicon antenna requires approximately 3kW of power and transmits RF between 7 and 50 MHz¹². The incident RF ionizes the fuel that flows into the second chamber at a sonic speed of 20 km/s. The second chamber is responsible for the acceleration of the ions in the plasma. The ions, much heavier than

¹¹ Chang Diaz, F.R, et al. "An Overview of the VASIMR Engine: High Power Space Propulsion with RF Plasma Generation and Heating", Invited Paper, American Institute of Physics 14th Topical Conference on RF Power in Plasma, Oxnard, CA, May 8, 2001.

¹² Chang Diaz, F.R. et al, "The Physics and Engineering of the VASIMR Engine," AIAA-2000-3756, 3.

the electrons, are accelerated by the RF tuned to the ion resonance frequency (13.65 MHz for He and 25 MHz for H)¹³. This ion cyclotron resonance heating (ICRH) only adds energy to the velocity component perpendicular to the magnetic field lines. Superconducting magnets around the outside of the chamber establish a magnetic beach or choke, that allows only the highest energy ions to leave the second chamber. Magnetic mirroring contains the lower energy ions in the second chamber and allows them greater exposure to the ICRH. Once the ions have adequate total energy, enough to maintain some velocity parallel to the magnetic field, they are ejected into the third chamber. This third chamber consists of a diverging magnetic field that emulates a Laval rocket nozzle. As the plasma travels aft, β increases above unity and the flow transitions to super-alfvénic flow. Super-alfvénic flow occurs when the plasma is traveling faster than the characteristic speed of hydromagnetic perturbation waves, similar to supersonic flow in gases. Most of the cyclotron speed of the ions has been converted to parallel velocity and the plasma has enough energy to stretch the magnetic field lines and detach.

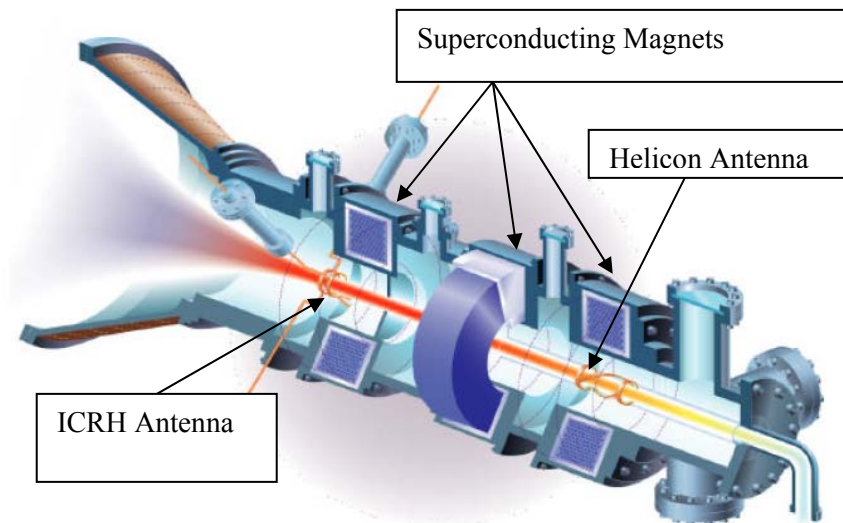


Figure 6. VX-10 Configuration

The phenomenon of exhaust plume detachment has created many unanswered questions. Due to the constraints of VX-10's central vacuum chamber pumps, the ions do

¹³ Chang Diaz, F.R. et al. "Experimental Progress Toward the VASIMR Engine," Invited Paper, 28th International Electric Propulsion Conference, Toulouse, France, March 2001, 1.

not have a continuous free-path exit. The chamber fills quickly with neutral particles, which act as a viscous fluid for the exiting plasma. This viscous resistance inhibits true thrust from being determined. Currently the only way to alleviate this condition would be to test the VX-10 in space. Some believe that radial particle loss due to anomalous transport prevents optimum thrust production¹⁴. These losses occur as the magnetic field lines confine some plasma constituents to remain attached to the engine's magnetic field lines. This decreases the total number of particles contributing to thrust. This thesis deals with the design and construction of a flux probe, one of three probes, that will be used by ASPL to determine ionization efficiency and explore the field-line dragging characteristics of a 20-kW VASIMR engine.

e. Field Line Dragging Experiment

The purpose of this experiment is to demonstrate that when super-Alfvénic plasma flow enters a region of weak magnetic field, the embedded field is dragged into the weak field region¹⁵. An Alfvén wave is a traveling oscillation of plasma ions and the magnetic field, similar to an acoustic wave in conventional rocket exhaust. Super-Alfvénic plasma is similar to supersonic exhaust flow in that disturbances and properties cannot propagate as fast as the flow. In this experiment, ASPL hopes to be able to discern the super-Alfvénic plasma capturing the magnetic field lines present in the plasma prior to the magnetic nozzle and moving them with the plasma into a weaker field region in the nozzle. This is the first step in showing that the plasma β is high enough to influence magnetic field lines and detach cleanly from the engine's magnetic field. The following diagram depicts magnetic field lines for a typical deuterium discharge and possible probe positions relative to those lines. The axis measurements are in meters. The z measurement is a location (meters) from the gas feed line at the beginning of the engine. M3 and M4 are the superconducting magnets. The coils consist of heavy gauge wire wound around the exhaust chamber and will be energized to either null or reverse the magnetic field lines.

¹⁴ Private Communication with ASPL's Dr. Tim Glover.

¹⁵ Glover, Tim "A Proposed Demonstration of Field-line Dragging in VASIMR", December 2004, 1.

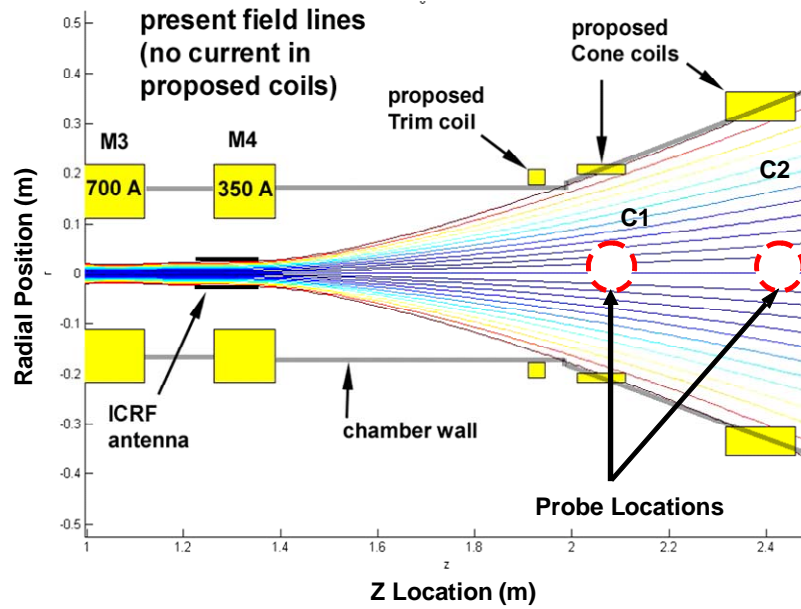


Figure 7. Normal Magnetic Field Lines

Figure 8 depicts the weak magnetic region that is created when current is applied to the coils. The “cusps” that are formed are a result of the interactions between the coils’ and VASIMR’s magnetic fields. The annotations “F. Cup” and “gaussmeter” refer to two other instruments that will be present during the experiment. The Faraday Cup (F. Cup) will measure ion flux and will calibrate the Langmuir probe amplitudes. The gaussmeter will measure the three components of the magnetic field.

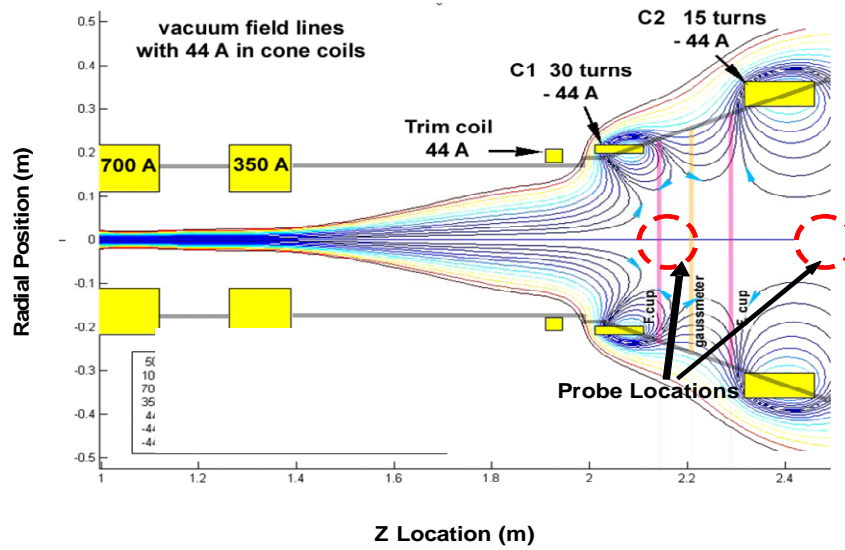


Figure 8. Weak Field Lines¹⁶

Figure 9 depicts the predicted field line dragging by the plasma into the weak magnetic field zone. The Langmuir probe should show a tighter collimation of the plasma as a result.

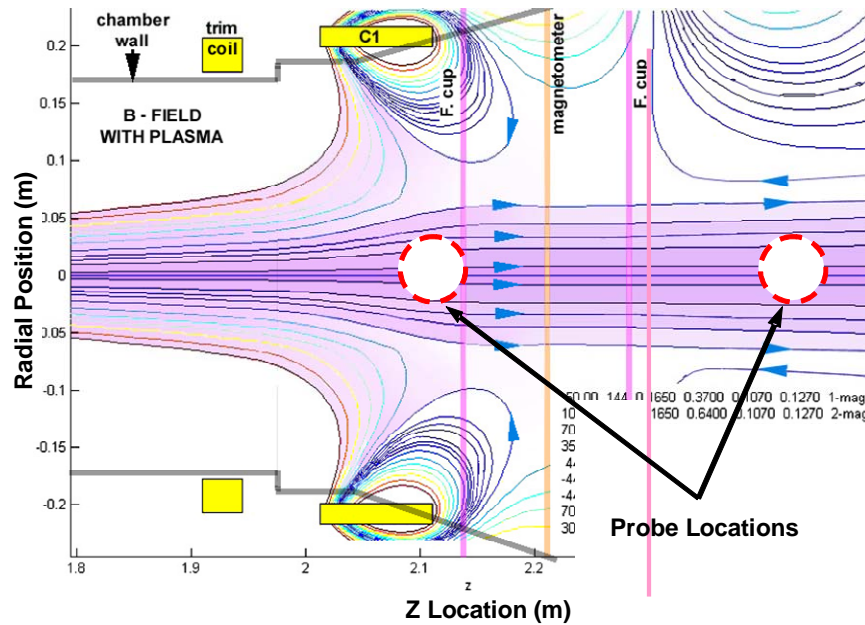


Figure 9. Plasma Dragging Lines into Weak Region¹⁷

¹⁶ Glover, Tim. "A Proposed Demonstration of Field Line Dragging in VASIMR," December 20, 2004.

When the current polarity is reversed in the coils, the generated magnetic field should cause a reverse orientation of the exhaust magnetic field, dramatically slowing the plasma. This is much like a magnetic exhaust valve. The Langmuir probe is expected to see a large drop in current density. Figure 10 depicts this condition. A complete copy of Dr. Tim Glover's experiment proposal is located in appendix B.

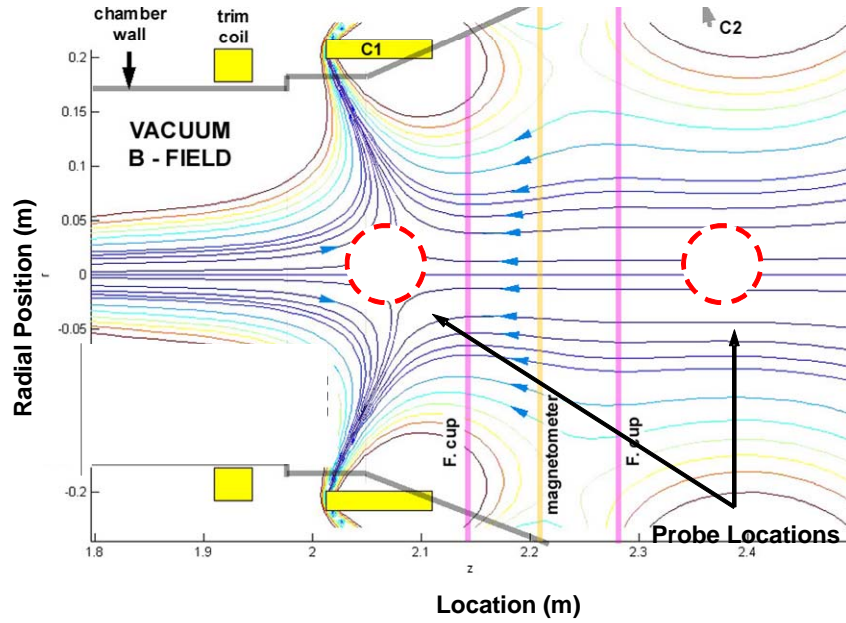


Figure 10. Reverse Polarity Coil Current¹⁸

¹⁷ Glover, Tim. "A Proposed Demonstration of Field Line Dragging in VASIMR," December 20, 2004.

¹⁸ Glover, Tim. "A Proposed Demonstration of Field Line Dragging in VASIMR," December 20, 2004.

II. LANGMUIR PROBE

A. BACKGROUND

1. History

In the 1920s, Dr. Irving Langmuir introduced the concept of electron temperature and developed a probe to measure it, a thermo-ionic or Langmuir probe. Since then, the Langmuir probe has been a widely used diagnostic tool, especially for plasmas. Physically quite simple, a conductor immersed in plasma, the complexity of the Langmuir probe lies in the interpretation of the results¹⁹. The interactions between an immersed probe and its surrounding plasma are not completely understood.

2. Theories Evolve

Since the inception of the Langmuir probe, several physicists have devised theories to describe the complex interactions of a conducting probe immersed in a plasma. Orbital Motion-Limited (OML) theory, partially developed by Langmuir, assumed that ion current is limited by angular momentum of the ions due to temperature. Between 1926 and 1956, many probe papers disagreed on the lengths between the sheath and quasi-neutral regions. In 1957, Allen, Boyd, and Reynolds (ABR) derived a differential equation that could determine plasma potential in all directions regardless of the sheath or pre-sheath. This theory is well suited to spherical probes and assumes that ion kinetic temperature is generally zero. This holds true for relatively cool plasmas consisting of mainly bulk flow. For finite ion temperature, the theory assumed that ions with small angular momentum would strike the collector, while those with larger angular momentum would miss the collector completely. These high-energy ions would not contribute to the ion density. In 1959, Bernstein and Rabinowitz (BR) solved this problem for mono-energetic ions. They surmised that the angular momentum is a potential barrier that must be overcome for the ions to impact the probe. Therefore some ions do not possess sufficient energy and become trapped in closed orbits around the

¹⁹ Hutchinson, I.H. *Principles of Plasma Diagnostics Second Edition*. (Cambridge Press, 2002) 55.

probe. Currently, no scientific data exists to support the existence of these trapped ions around any charged probe. This paper will subscribe to the generally accepted OML theory of ion collection.

3. Orbital Motion-Limited Theory

OML theory, as proposed by Langmuir, asserts that ions and electrons near a probe come from far away in the ambient plasma and will either fly past or directly strike the probe. Those that fly past return to the ambient plasma and will not orbit the probe²⁰. This theory neglects the effects of inbound ions losing linear momentum to collisions and being trapped in orbits around the probe. For simplicity in analysis the plasma will be considered collisionless and OML theory will hold true.

When a conducting probe is immersed in plasma, it develops a potential called the floating potential. It also becomes surrounded by a symmetrical cloud of oppositely charged particles called a sheath. Assuming that the gas pressure is low enough that the sheath particles do not impede free-path movement of plasma bulk flow, the current taken by the collector can be determined in terms of collector radius, Maxwellian velocity distributions of incoming particles, and the potential drop across the sheath. For example, assume that the collector's potential is biased negatively with respect to the plasma potential. The collector then repels electrons and attracts ions. A positively charged sheath will form symmetrically around the collector. The sheath dimensions are such that the total charge of the sheath will be equal and opposite to that of the collector. The electric field of the probe will not extend past the sheath. The current collected by the probe cannot exceed the rate at which ions arrive at the sheath edge due to their proper motions.

If the negative bias of the collector is large compared to the voltage equivalent of the ion velocities, then the sheath may be divided into two general regions. The center region has the highest potential drop between the gas and the collector and thus contains mostly positively charged ions and a few high velocity electrons. The outer region will contain an equal share of electrons and ions. The population of ions will move to the

²⁰ Langmuir, Irving et al., "The Theory of Collectors in Gaseous Discharges," *Physical Review*, (October 1926), 727.

center region to replace ions absorbed into the collector. The two regions merge into each other, depending upon the velocity distribution of the ions. The potential of the outer region will asymptotically reach the plasma potential, thus the sheath does not have a sharp edge. The potential drop in the outer region is considerably smaller than the total drop, so many define the sheath edge as the surface of the sharp potential drop.

Another common assumption is that the gas pressure is so low that a minimal number of collisions occur within the sheath. The ions in the sheath move in free orbits, some of which end on the collector. If the sheath has axial symmetry so that the equipotential regions form concentric cylinders, then the condition for a particle to reach the probe face depends only on the potential drop across the sheath and the velocity before entering the sheath²¹.

4. Operation

Parameters such as electron temperature, plasma potential, and plasma density, can be determined by observing the current from the probe as a function of the potential difference between the probe and plasma space potentials. The product is a curve called the probe characteristic. The ion saturation region is located to the left of the neutral bias line ($V=0$) and shows when a continuously decreasing negative bias produces a relatively steady probe current. The electron saturation region is the region on the opposite side of the neutral bias line showing the same phenomenon except with electron collection.

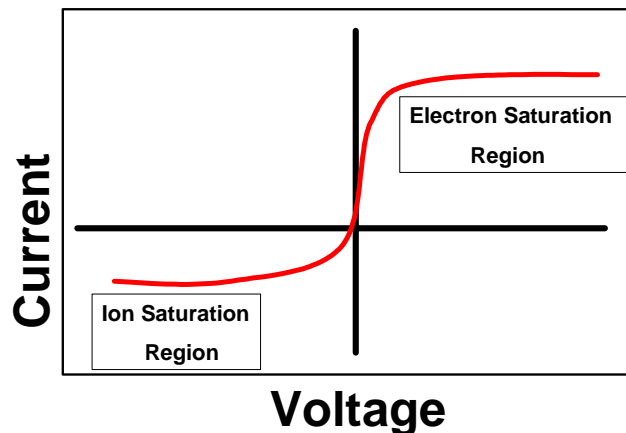


Figure 11. Characteristic Curve

²¹ Langmuir, Irving et al. "The Theory of Collectors in Gaseous Discharges," *Physical Review*, (October 1926), 743.

The probe current is a result of the various plasma species (electrons and ions)

$$I = A \sum_i n_i q_i v_i$$

where A is total collecting surface area, q is the particle charge, n is the number density, and v is the average particle velocity. We also know that

$$\bar{v} = \frac{1}{n} \int v f(\bar{v}) d\bar{v}$$

where

$$f_\alpha(\bar{v}) = n \left(\frac{2\pi KT_\alpha}{m_\alpha} \right)^{-\frac{3}{2}} \text{Exp} \left(\frac{-\frac{1}{2} m_\alpha |\bar{v}|^2}{KT_\alpha} \right)$$

which is known as the Maxwellian distribution function. This function is used to evaluate the velocities in each direction. The current to the probe from each particle (in every direction) is

$$I(v) = nqA \int_{-\infty}^{\infty} dv_y \left(\frac{2\pi KT_\alpha}{m_\alpha} \right)^{\frac{1}{2}} \text{Exp} \left(\frac{\frac{1}{2} m_\alpha v_y^2}{KT_\alpha} \right) \bullet \int_{-\infty}^{\infty} dv_z \left(\frac{2\pi KT_\alpha}{m_\alpha} \right)^{\frac{1}{2}} \text{Exp} \left(\frac{\frac{1}{2} m_\alpha v_z^2}{KT_\alpha} \right) \bullet \int_{v_{\min}}^{\infty} dv_x \left(\frac{2\pi KT_\alpha}{m_\alpha} \right)^{\frac{1}{2}} \text{Exp} \left(\frac{\frac{1}{2} m_\alpha v_x^2}{KT_\alpha} \right)$$

where $v_{\min} = \left(\frac{2qV}{m_\alpha} \right)^{\frac{1}{2}}$

any particle with less than v(min) will be repelled. The probe consists of flat, parallel collector plates that are oriented opposite to bulk flow direction. Thus, the integrals in the z and y directions equal unity so the current of a z, y plate facing an x-direction plasma flow will experience a current

$$I(v) = nqA \int_{v_{\min}}^{\infty} dv_x v_x \left(\frac{2\pi KT_\alpha}{m_\alpha} \right)^{\frac{1}{2}} \text{Exp} \left(\frac{\frac{1}{2} m_\alpha v_x^2}{KT_\alpha} \right)$$

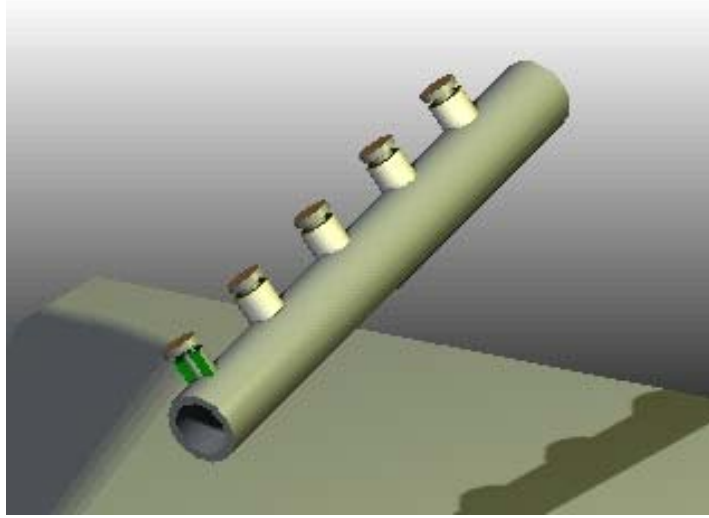


Figure 12. Collector Plate Orientation

In this current density and flux investigation, both ion and electron saturation current could be used to determine density. However, electron saturation current is so high that it could cause damage to the probe or its attached circuitry. Therefore, ion saturation current will be collected by negatively biasing the probe with respect to the plasma potential. To repel most of the free electrons, the voltage bias must be several times KT_e or approximately 50 V below the plasma potential²². Approximate ion saturation current, also called Bohm current, is defined as

$$I_B = \frac{1}{2} neA \left(\frac{KT_e}{m_i} \right)^{\frac{1}{2}}$$

where n is ion density, m_i is ion mass, and e is the particle charge²³.

When the charged probe is inserted into the plasma, a sheath will form around it. For typical VASIMR parameters, the Debye length is approximately 0.15mm and the sheath width can be as large as five Debye lengths or 0.75mm. The collector plates are large enough (diameter of 6.35 mm) that the sheath thickness is very small (only 10% of probe dimensions). This thin-sheath approximation is commonly used with Langmuir probes and states that the sheath area is effectively the same as the probe area for high

²² Private Communication with Dr. Tim Glover.

²³ Chen, Francis F. *Introduction to Plasma Physics and Controlled Fusion*, Second Edition, (Plenum Press, New York) 296.

density plasmas. At low densities, λ_D can become large enough that some ions entering the sheath will orbit and never impact the probe surface. VASIMR plasmas are considered high density ranging from $10^{17} - 10^{19} \text{ m}^{-3}$ ²⁴.

The probe consists of six, evenly spaced tungsten collector plates. Ion bombardment of these plates will create six positive currents that can be determined by measuring the voltage across sensing resistors. Each voltage is filtered by an isolation amplifier and sampled by a data acquisition computer (DAQ) with a frequency of 5000 Hz (as depicted in Figure 13).

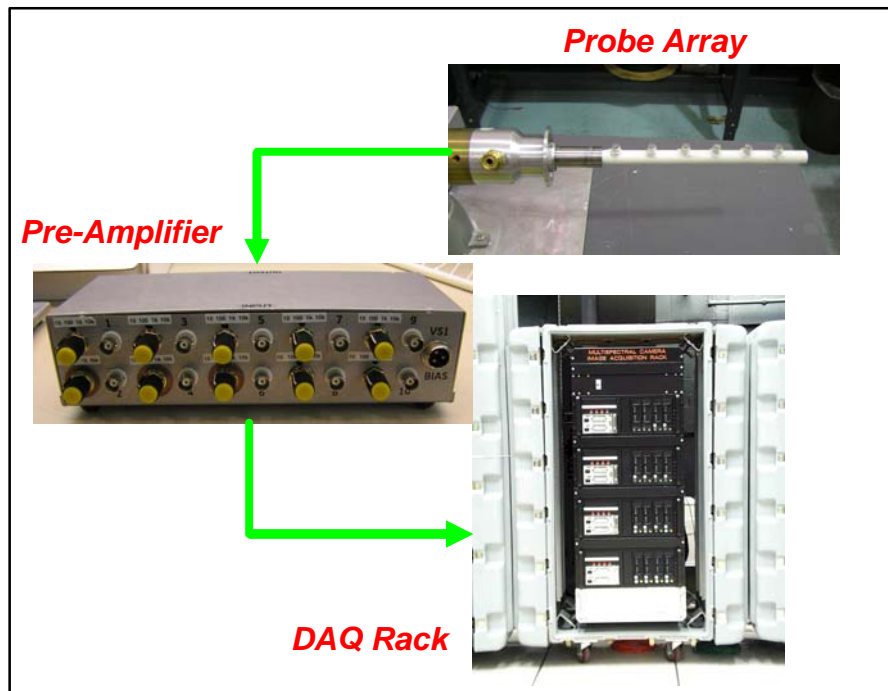


Figure 13. Experimental Set Up

B. CONSTRUCTION

1. Location and Size

The array of probes is designed to investigate plume characteristics at two ports aft of the last magnet. The following diagram shows where in the exhaust the probe will

²⁴ Chang Diaz, F.R. et al "Helicon Plasma Injector and Ion Cyclotron Acceleration Development in the VASIMR Engine" AIAA-2000-3752, 1.

be inserted. All locations in the VASIMR engine are measured in centimeters from the fore-most portion (the fuel supply valve) of the engine.

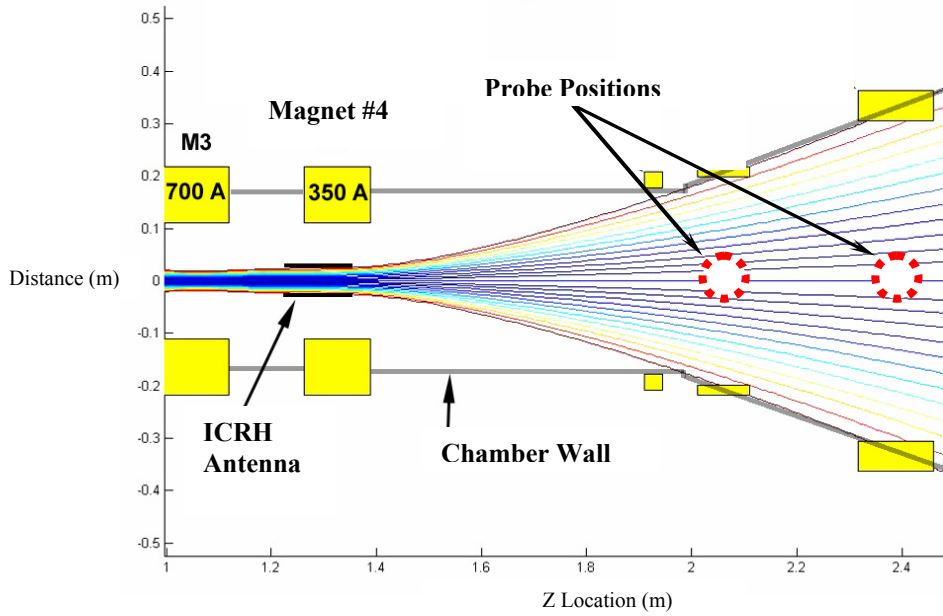


Figure 14. Diagram of Probe Placement²⁵

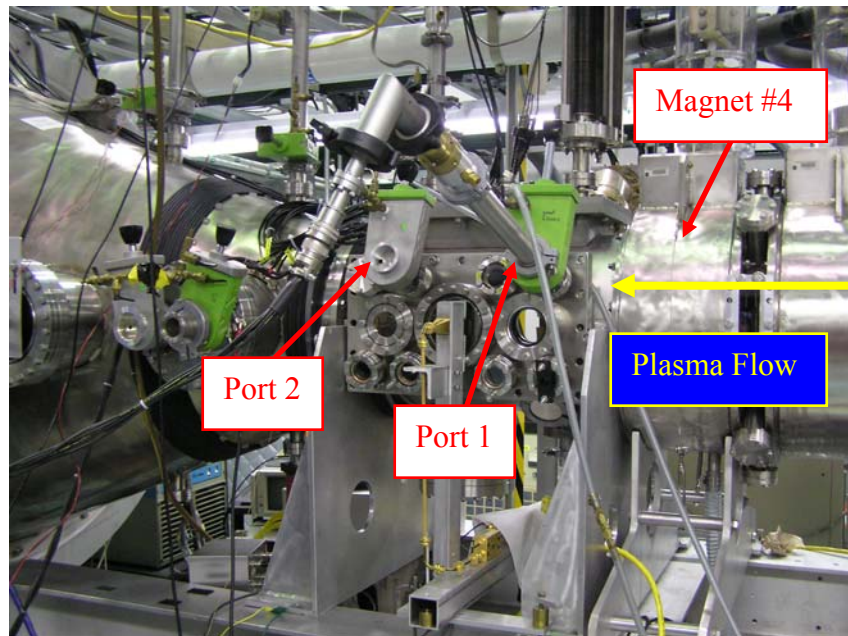


Figure 15. Gate Valves Used to Insert Probe

²⁵ Glover, Tim. "A Proposed Demonstration of Field Line Dragging in VASIMR," December 20, 2004.

To determine the actual length of the probe, approximate plasma densities were charted as a function of distance from the fourth magnet. The following chart describes plasma characteristics of each port, including its location, magnetic field strength, peak plasma density, plume radius, associated Debye and sheath lengths, and the required probe size to ensure a thin-sheath assumption. The magnetic field strength was measured during previous VASIMR experiments. The peak density and plume radius were predicted values, an output from computer simulations written by ASPL scientists. All chart distances are measured in centimeters.

Port	Z	B(T)	Npeak (cm ⁻³)	Plume Radius	Debye Length	Sheath Length	Probe Radius	Probe Diameter
1	207	0.0022	8.80E+10	12.11	0.007	0.028	0.354	0.708
2	242	0.001	4.00E+10	17.96	0.011	0.042	0.525	1.051

Table 1. Port Characteristics

The Z measurement is the engine longitudinal coordinate measured from the fuel source at the beginning of the engine. The magnetic field strength is measured in Tesla. Npeak is the predicted ion density at a particular downstream distance in the exhaust. The radius is the estimated effective radius of the exhaust plume. At this distance, the density is expected to rapidly decrease outward, marking the edge of the plume. The sheath length is approximated at four times the Debye length (λ). To be able to assume a thin sheath, the probe diameter should be about 50 times the Debye length. This ensures that the sheath will never be larger than the physical area of the collector and the collection area will not change as the bias voltage is varied. Based on the calculated diameters and availability of material, a 0.635 cm (0.25”) diameter disc will be used as the collector. These six collectors will be evenly spaced over approximately 30 cm (one foot).

2. Material Selection

The probe will be bombarded by high-energy plasma electrons and ions. The electrons will impact the surface and transfer some of their momentum to other resident electrons. Sometimes the energy transfer is high enough to eject electrons from the metal surface. This will create a positive charge and falsely increase the ion current from the probe. This phenomenon is characterized by the secondary electron emission coefficient, δ , which is a ratio of the average number of surface-emitted electrons per incident

electron. Ideally, one would prefer a δ of unity or less. This will ensure that the number of electrons entering the surface will equal to or greater than the number being emitted.

Ion sputtering is another concern when choosing collector material. Sputtering is the displacement of host atoms by high-energy incident ions. The host atoms are knocked free from their crystalline structure and ejected into the vacuum environment. This process is quite similar to erosion, but happens on a compressed timeline. Sputtering can cause rapid collector deterioration, destroying the uniformity of the collectors. This lack of uniformity would skew the results as the collector areas would no longer be the same. Sputter threshold is the minimum kinetic energy of incident particles needed to dislodge resident atoms.

The collector must be made from a material that has both a low secondary electron emission coefficient (SEEC) and low ion sputter characteristics. The material must also be able to withstand the high temperature of the plasma for the duration of the VASIMR shot (2-3 seconds) and have a low coefficient of thermal expansion. The refractory metals, Tungsten (W), Tantalum (Ta), Rhenium (Re), Niobium (Nb), and Molybdenum (Mo) all exhibit these characteristics. They are also excellent choices for an electrode because of their low, uniform surface potential and high resistance to oxidation. The following table contains each metal's pertinent characteristics

Element	Symbol	Sputter Threshold(eV)	SEEC	Z	Coeff Th Exp (um/C)	Melting Point (C)	Density (gm/cc)
Copper	Cu	7	0.8	29	16.5	1084	8.92
Molybdenum	Mo	8	0.8	42	4.9	2610	10.22
Niobium	Nb	9	0.6	41	7.3	2468	8.57
Rhenium	Re	10	0.8	75	6.2	3180	21.02
Tantalum	Ta	13	0.4	73	6.5	2996	16.65
Tungsten	W	13	0.3	74	4.3	3410	19.33

Table 2. Element Properties^{26,27,28}

²⁶ Webelement's Periodic Table: Professional Edition
<http://www.webelements.com/webelements/elements/text/Nb/heat.html> (accessed October 20, 2005)

²⁷ Cougar Labs, Inc. <http://www.cougarlabs.com/sput1.html> (accessed November 8, 2005)

²⁸ Lieberman, Michael A. and Allan J. Lichtenberg, *Principles of Plasma Discharges and Materials Processing*. John Wiley and Sons, Inc. NY, NY, May 1998.

After balancing several factors including availability, machinability, SEEC, and sputter characteristics, Tungsten was chosen over Copper and the other refractory metals. As seen from the table, Tungsten has the highest melting point and lowest thermal expansion coefficient. This helped to ensure uniformity between the six different discs. To further ensure collector area uniformity and protect wiring, the back of the tungsten plates have a ceramic collars. The ceramic helps to prevent collection of ions not associated with the bulk flow of the plasma. Despite the high plasma velocity, some ions could travel across stream or even upstream due to complex interactions in the plasma shadow. The ceramic collar also protects the solder connection between the plate and the wire leading out of the chamber from the same impinging ions (as depicted in Figure 16).

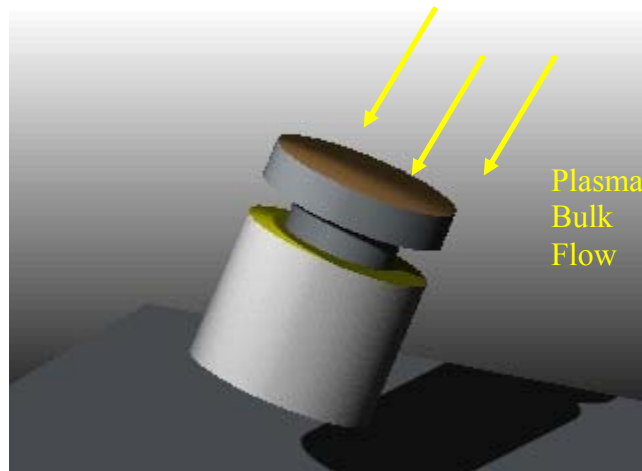


Figure 16. Tungsten Collector Plate With Ceramic Collar

A glass ceramic called Macor is the material of choice. It was chosen for its relative ease of machinability, high electrical resistivity, low coefficient of thermal expansion, and inert characteristics in the plasma/vacuum environment. The only disadvantage to Macor is the arcing that occurs at a metal/Macor interface immersed in plasma. To mitigate this undesired trait, the Macor collar's radius (behind the collector) will be slightly smaller. This will prevent the interface from being directly exposed to the plasma bulk flow. Figure 17 shows the final Macor-collector construction.

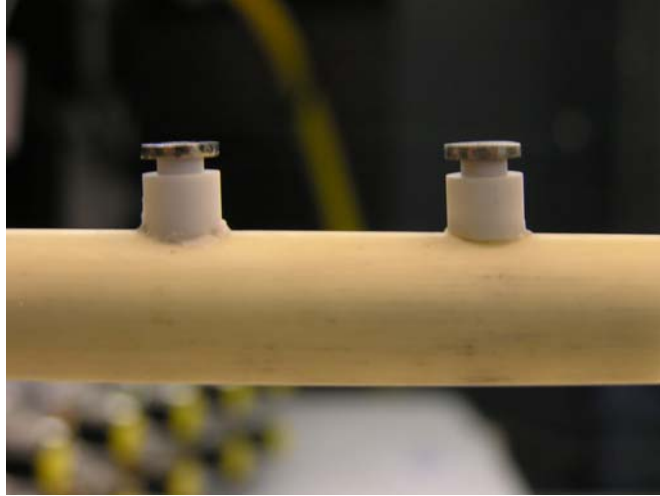


Figure 17. Actual Probe Discs With Macor

Each of the Macor collars will then be attached to a hollow rod that houses the wires. Alumina or Aluminum Oxide (Al_2O_3) is a highly versatile refractory ceramic oxide that is commonly used in VASIMR operations. The close structural packing of the aluminum and oxygen atoms leads to a high refractive index, low coefficient of thermal expansion, and high melting point.

3. Manufacture and Assembly

Two probes and pre-amplifier circuits were designed and built. The first, a mere prototype, consisted of two discs and two pre-amp circuits. This was tested early in the experimentation to validate material and component selection. After prototype verification, construction began on the final probe consisting of six discs. This section will speak to the final probe construction.

The machinable Tungsten discs are 0.635 cm in diameter to ensure that a thin sheath approximation is applicable. This diameter corresponds to a readily available stock of 0.25" Tungsten rods. The discs need some mechanical support to ensure proper collector orientation, so they are designed with a neck that protrudes from the back of the disc. This neck extends through the Macor collar and is silver soldered to the signal wire resident in the alumina tube. This type of solder is mechanically rigid and will not outgas when exposed to the "hard vacuum" (10^{-5} Torr) of the VASIMR chamber. The following

is a schematic of the disc, a cut-away collar, and a solid collar. The dimensions are in English units due to a limitation of ASPL's lathe.

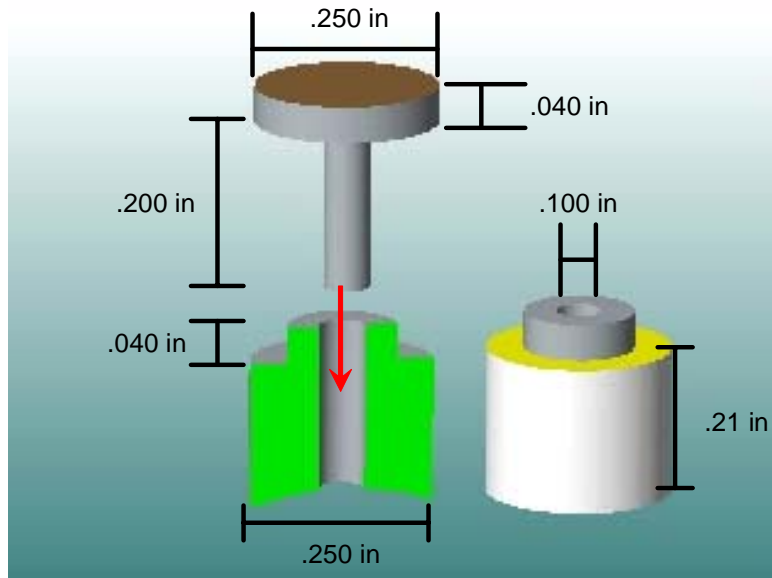


Figure 18. Collar and Disc Dimensions

The collars are attached to the back of the discs and alumina tube using Torr Seal adhesive. This adhesive was used for its low out-gassing and high-temperature characteristics. The orientation of each disc is critical to ensure uniformity of the probe. Flat mounting each disc to its Macor collar required a constant pressure while the adhesive cured. The discs were placed face-down on a workbench. An acrylic guide form secured each Macor collar in place. A piece of wood was then placed on top of the acrylic and pressure was applied with a vice. Below is a picture of the rig used to ensure a uniform flat mounting.



Figure 19. Disc and Collar Mating

The next step was mounting the disc/collar assemblies on the alumina tube. The tube was placed flat on the workbench, then the same piece of acrylic was used to align the disc/collar assemblies on the alumina rod. Adhesive was added to the collar tube interface. Holding pressure was supplied by adding tension to the coaxial wires connected to each disc. The following picture shows the final collector plate orientation.



Figure 20. Collector Orientation

Coaxial wires carry the current away from the collector plates and out of the vacuum to the pre-amplifier and LC filters. The outside conductors of the 28 AWG coaxial wires are grounded to the chamber and act as RF shields for the saturation current. Each of the six coaxial wires is soldered to a corresponding feedthrough rod that allows the current to pass out of the vacuum chamber to the data acquisition (DAQ) hardware.

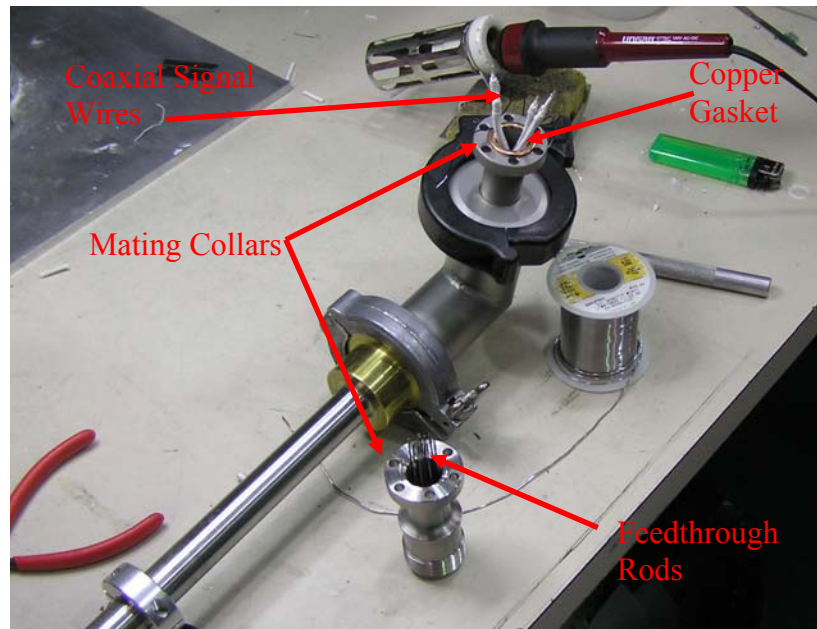


Figure 21. Feedthrough and Signal Wires

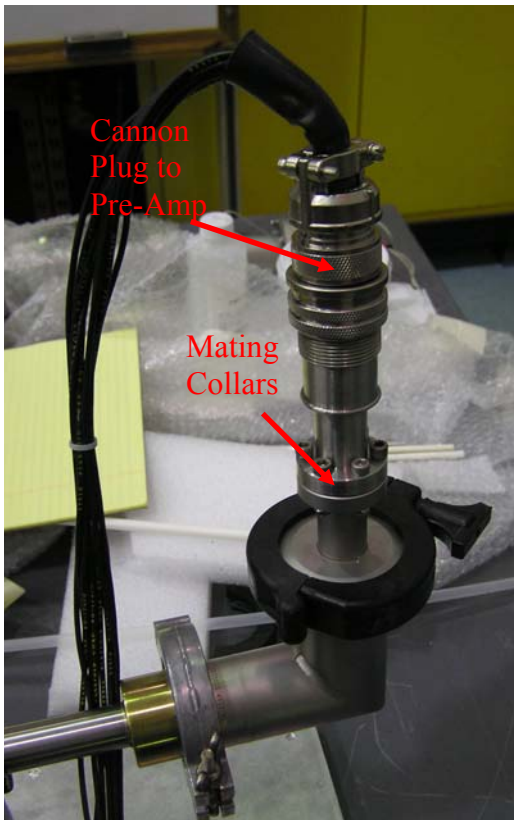


Figure 22. Complete Feedthrough with Cannon Plug

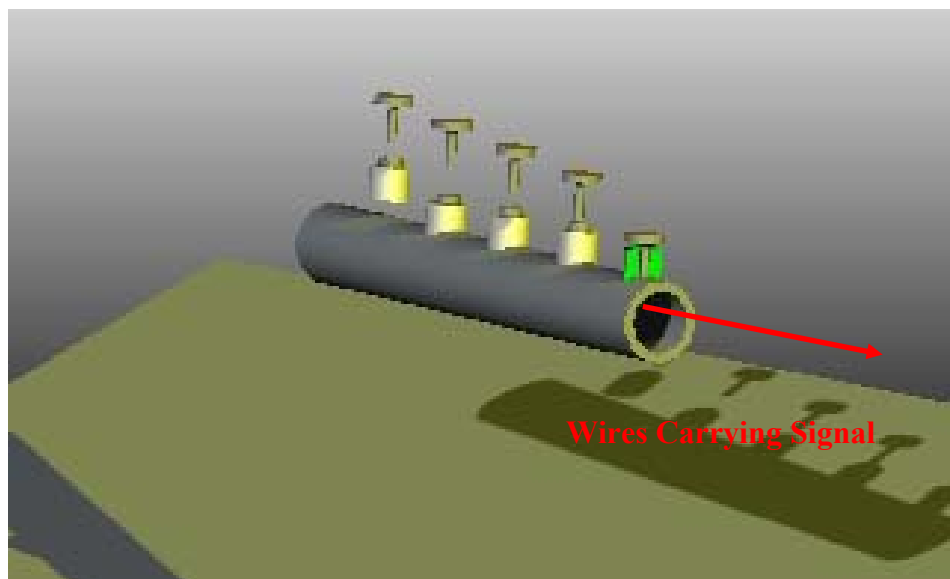


Figure 23. Model of Total Probe Construction



Figure 24. Complete Probe Construction

4. Pre-Amplifier Construction

a. Isolation Amplifier

To protect the DAQ hardware, the ion saturation current cannot be directly connected to the equipment. Fear of spurious current peaks during plasma initiation requires a capacitive barrier between the ion current and the collection computers. The saturation current is drawn through a resistor. The voltage across this sensing resistor is the input to the isolation amplifier. The prototype pre-amplifier circuit was based on Analog Devices' AD215 Isolation Amplifier.

The AD215 is a high-speed input amplifier designed to isolate wide bandwidth analog signals. It provides complete galvanic isolation between the input and output of the pre-amp and includes front-end isolated power supplies. These $\pm 15\text{V}$ supplies prevent the need for an isolated DC/DC converter and thus simplify circuit design. The AD215 has a typical full-power bandwidth of 120 kHz, rise time of $3\ \mu\text{sec}$, settling time of $9\ \mu\text{sec}$, and gain of unity. This large bandwidth and rapid system response will easily accommodate the dynamic ion saturation current while the gain will not distort the signal. The signal is further conditioned with an op amp at the input and capacitive barrier output of the AD215. This op amp acts as an electronic buffer and helps to ensure crisp, clear voltage changes. The following is a functional block diagram of the AD215.

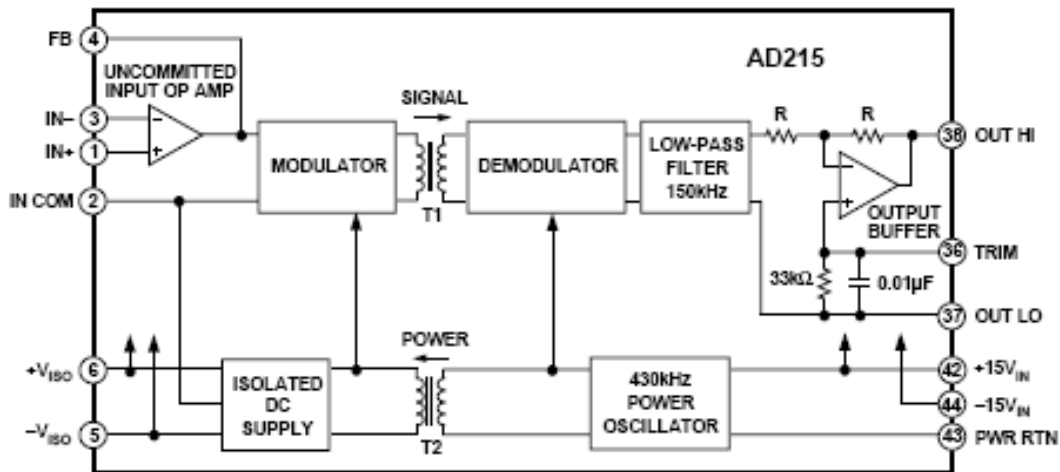


Figure 25. Block Diagram of AD215

The complete prototype pre-amp circuit consisted of four sensing resistors (to vary circuit sensitivity based on ion saturation current), two isolated voltage sources replete with buffer capacitors, and a trim potentiometer to vary output voltage offset. The standard output offset of the AD215 is -35mV. The trim potentiometer can correct this offset to 0 mV. This helps to ensure that the output voltage matches the voltage drop across the sensing resistor. Below is a schematic of the pre-amp.

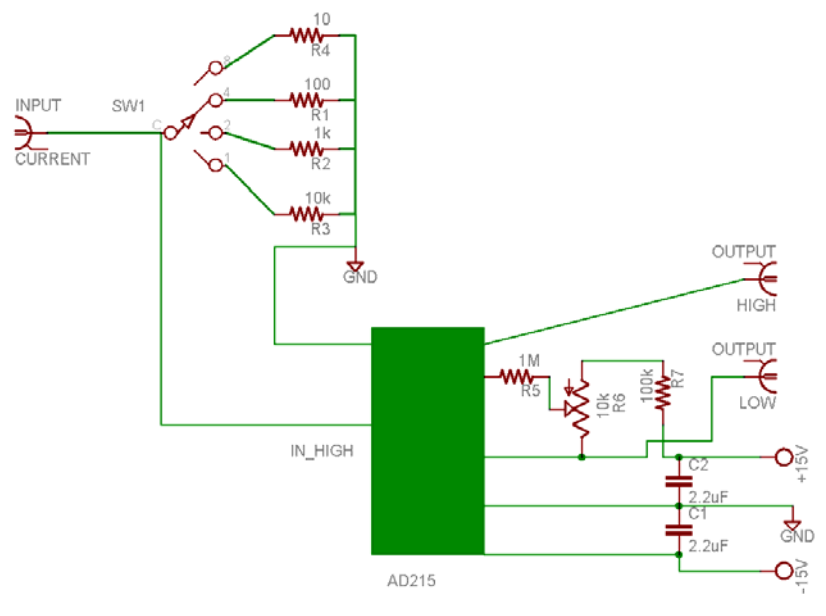


Figure 26. Prototype Pre-Amplifier Schematic

The above circuit worked well and was tested with a gradually increasing frequency signal. The output signal matched the input signal up to 110 kHz. Unfortunately the supply chain of AD215s from Analog Devices became dangerously low. The production timeline for new AD215s did not fit the experimental plan, so an alternative had to be found.

After searching various parts' specification sheets, a suitable, low-cost alternative to the AD215 was found and implemented -- Texas Instruments ISO124 Precision Isolation Amplifier. The ISO124's input and output sections are galvanically isolated by two matched 1pF isolating capacitors that are encased in a plastic package. The input is duty-cycle modulated and digitally transmitted across the barrier. Using this technique, barrier characteristics do not degrade signal integrity which allows for excellent reliability and great high-frequency transient immunity across the barrier. The output section receives and converts the signal back to an analog voltage and removes the ripple component. This precision amp needs no external components to operate, but does require two isolated power sources (unlike the AD215). At a fraction of the cost of the AD215 and more than adequate availability, the ISO124 was an easy choice. With a smaller bandwidth of 50 kHz, the ISO124 would cut out more of the noise from the raw signal. The longer settling time of 50 μ sec was adequate in accurately determining ion saturation current fluctuations. Below is a simple wiring diagram for the ISO124.

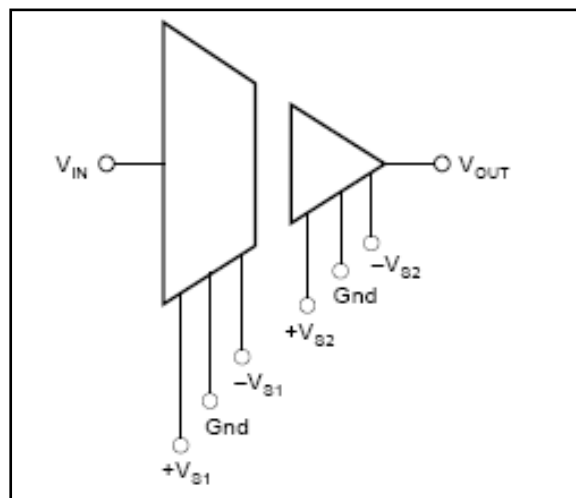


Figure 27. ISO124 Wiring Diagram

The response bandwidth was optimal to the experiment as it was smaller than the AD215's. The ion current was expected to have component frequencies no higher than 1 kHz. The ISO124's 50 kHz helped to block out more of the RF noise. The isolation voltage of the pre-amp never went above 50V (probe bias voltage). Both signal frequency and isolation voltage were well within the performance curve of the ISO124.

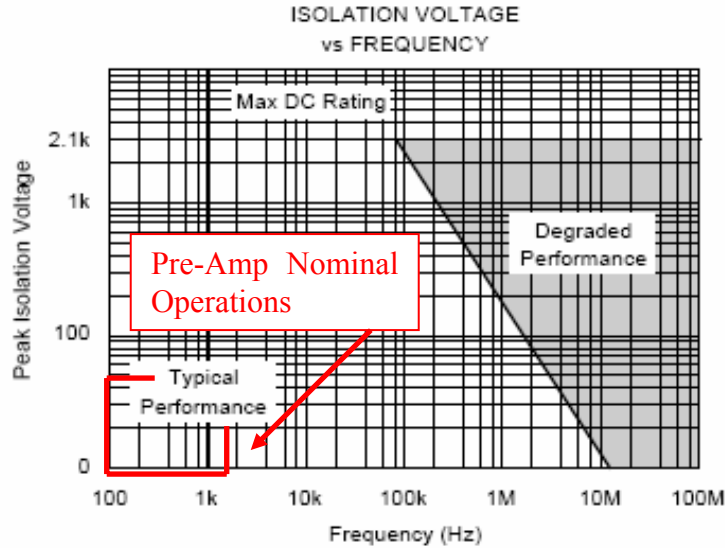


Figure 28. ISO124 Performance Curve

b. Sensing Resistors

The ion current is translated into a voltage signal across a selectable sensing resistor. The resistor value is based on the magnitude of the incoming current according to Ohm's Law,

$$V = IR$$

The expected probe current is the Bohm current, as previously discussed,

$$I_B = \frac{1}{2} neA \left(\frac{KT_e}{m_i} \right)^{\frac{1}{2}}$$

The ion density (n) varies radially in the plasma. As the probe is placed further downstream, the radial density profile will change dramatically as the flow expands. Below is a table of predicted ion saturation currents and necessary resistance to ensure a

voltage signal between 0 and 5V. The predicted current is based on a simulation of VASIMR's current density profile and the collector effective area. This voltage envelope is determined by the input value range of the DAQ.

Plasma Density (m ⁻³)	Ion Current (A)	Resistance(Ohm)	Signal (V)
5.00E+16	0.003	1000	3.42
5.00E+17	0.03	100	3.42
5.00E+18	0.34	10	3.42
5.00E+19	3.42	1	3.42

Table 3. Resistance Values and Resulting Signal Voltages

The resistors used had a 2% tolerance to increase accuracy and a 1-Watt rating to ensure that each resistor would not burn out during experimentation. Table 4 lists the final resistor values for the pre-amplifier circuit.

Channel	R1(Ω)	R2(Ω)	R3(Ω)	R4(Ω)
1	1.3	10.1	99.5	0.992k
2	1.1	10.6	99.6	1.07k
3	1.3	10.2	99.8	1.067k
4	1.1	10	99.7	1.066k
5	1.2	10.2	99.6	1.069k
6	1.1	10	99.9	1.066k
7	1.2	10.2	99.6	1.065k
8	1.1	10.1	99.6	1.073k
9	1.3	10.2	99.4	1.07k
10	1.1	10.1	99.3	1.071k

Table 4. Sensing Resistor Values

c. LC Filter

A low-pass LC filter was added “downstream” of the ISO124 to eliminate additional low-frequency noise. The LC filters were built using a capacitor connected in parallel to a grounded inductor. The values of the components were based on the equation

$$f_{co} = \frac{1}{\pi * \sqrt{LC}}$$

where f_{co} is the cut-off frequency (in Hz) and L is the inductance (in Henry) and C is the capacitance (in Farads). Table 5 lists LC combinations that were used to find an adequate low-pass filter.

Inductor (H)	Capacitor(F)	Cut Off Freq (Hz)
0.01	5.00E-05	4.50E+02
0.01	6.00E-05	4.11E+02
0.01	7.00E-05	3.80E+02
0.01	1.00E-05	1.01E+03

Table 5. LC Filter Values

After careful examination of the output signal with the various low-pass filters, the cut-off frequency of 1 kHz eliminated the most noise without filtering any core components of the signal. Most of the RF noise that was filtered out was associated with harmonics of the 60 Hz power supply to the helicon antenna. Figure 29 is the schematic of the pre-amplifier circuit and pictures of the completed circuit.

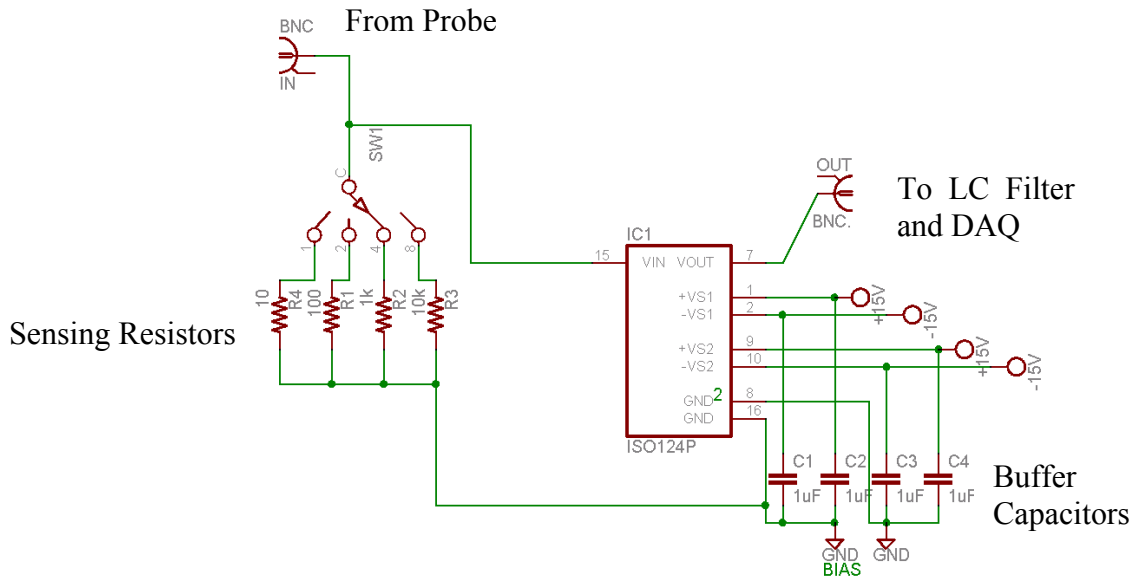


Figure 29. Pre-Amplifier Schematic

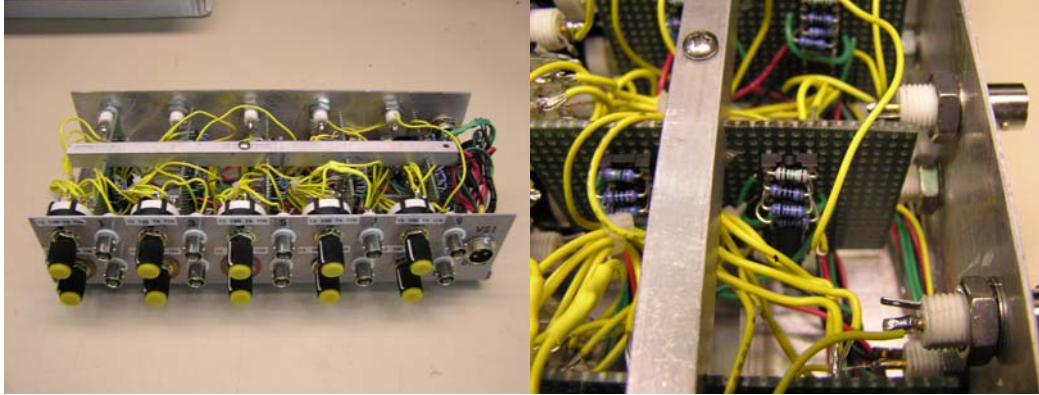


Figure 30. 10 Circuit Pre-Amp Box

The final pre-amp consisted of 10 isolation amplifier circuits each with four selectable sensing resistors with values of 1, 10, 100, and 1k Ohms (as seen in Figure 30). The yellow tipped knobs allowed the selection of each resistor. The yellow wires carried the signal while the black, green, and red wires were the negative, ground, and positive power wires for each ISO124 chip respectively. A buffer capacitor was connected to each power source to protect each ISO124 from current transients. Standard BNC connectors were used to connect the pre-amp circuits to both the probe input and the LC filters.

5. Calibration

The sensing resistor values were all checked using a voltmeter before installation. All values were within the advertised tolerance of 2%. After construction of all ten ISO124 circuits in the pre-amplifier, the path resistance was measured for each resistor in each circuit from the high potential side of the resistor to the pre-amplifier ground (“sensing circuit”). The Fluke 77 multimeter available for experimentation was much more accurate measuring voltage than it was measuring resistance. The total circuit resistance was determined by building a voltage divider circuit. A resistor of known resistance ($\pm .001 \Omega$) was placed in series with each of the sensing circuits. By measuring the voltage drop across the high-precision resistor and dividing that value by the known resistance, the current could be determined. The voltage of the sensing circuit was measured and divided by the calculated current to determine the sensing circuit resistance. Each of the 40 sensing circuits were sampled ten times with slightly different

source voltages. The average of the ten values became the accepted resistance of each sensing circuit or effective resistance of each sensing resistor.

A known current was then introduced through the input of the pre-amp box. The voltage across each sensing circuit was compared to the measured voltage at the output of the pre-amp box. Unfortunately the values did not agree past the tenths units. This created some unwanted instrument error. To correct this error, each sensing circuit voltage and output was measured 10 times with varying input current. Linear regression produced a first-order equation that would relate output voltage to the actual voltage across the sensing circuit. These first-order equations were then incorporated into the data analysis algorithms.

THIS PAGE INTENTIONALLY LEFT BLANK

III. RESULTS/ANALYSIS

A. RAW DATA

The raw data voltages were transferred from the pre-amplifier box to the DAQ computers via shielded cables. These cables were shielded from RF noise which is predominant all around the VASIMR test bed. Each collector's voltage signal was stored in a separate array. Each array had 8192 (2^{13}) addressable memory blocks. The average VASIMR shot duration for this experimentation lasted approximately 0.9 seconds. A sampling rate of 10 MHz allowed the voltage signals to be recorded from 0.0 to 0.82 seconds. The voltage sampling range for the DAQ is $-5V$ to $+5V$. Despite the in-line low-pass LC filter and the ISO124 cut off frequency of 50 kHz, the resultant signal was still too noisy to attain a distinct signal. Below is the raw data return from one of the collectors.

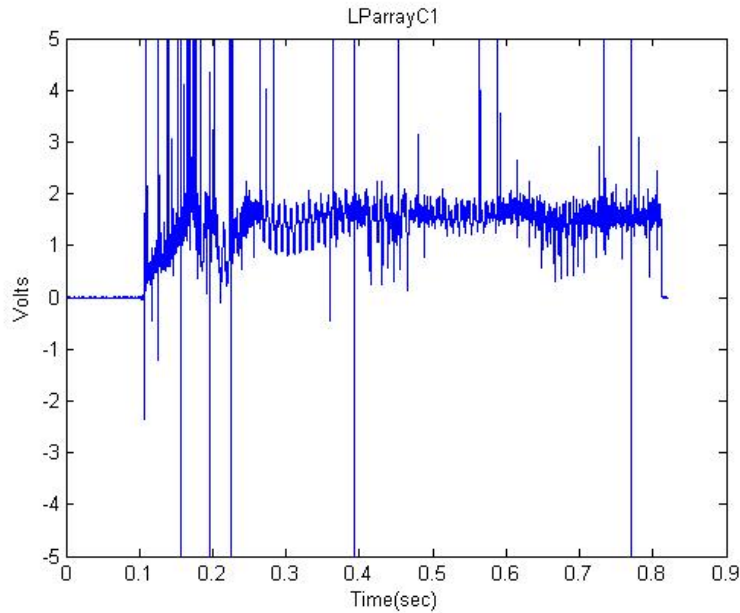


Figure 31. Noisy Raw Data from Collector#1

B. ANALYSIS ALGORITHMS

MATLAB 7.0 and its associated signal processing toolbox were used exclusively to recover signals and perform necessary calculations to produce the results of current density and flux. The actual script files can be found in appendix A.

1. Noise Filter

The noisy signal returns require further digital filtering to recover a useable signal. Two approaches were investigated to produce the highest signal to noise ratio. The first approach used MATLAB's zero-phase forward and reverse digital filtering. This function filters the data in each channel according to the difference equation

$$y(n) = b_1 * x(n) + b_2 * x(n-1) + \dots + b_{nb+1} * x(n-nb) - a_2 * y(n-1) - \dots - a_{na+1} * y(n-na)$$

where vectors a and b are user-defined and describe the numerator and denominator coefficients of the second-order transfer function respectively. This type of filter is also known as a direct form II transposed filter (DF2T). The DF2T is a common infinite impulse response (IIR) filter used in digital signal processing. This type of filter is known as IIR because it contains feedback. The main advantage of using an IIR is that it can achieve a given filtering characteristic using less memory and calculations than its finite impulse response (FIR) counterpart. Below is a schematic of such a filter:

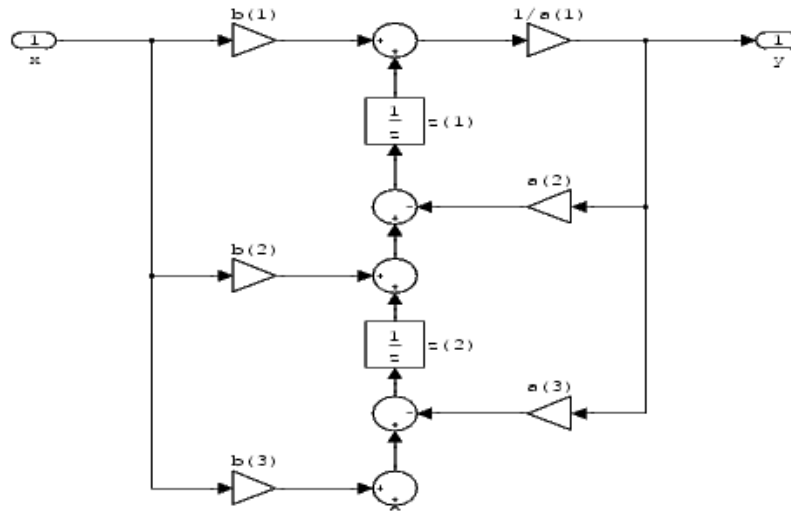


Figure 32. Direct Form II Transposed Filter

The vector is first filtered in the forward direction, then re-filtered in the reverse direction. The final product is the time reverse of the output after the second filtering operation. This product has zero phase distortion and the magnitude is modified by the square root of the filter's magnitude response.

In more practical terms, the DF2T filter is similar to boxcar averaging found in signal processing. If the a vector consists of all ones, the b vector determines over how many adjacent points each value will be averaged. In this case, 40 points seemed to adequately filter out the signal. Below is a representation of the original signal with DF2T filtering.

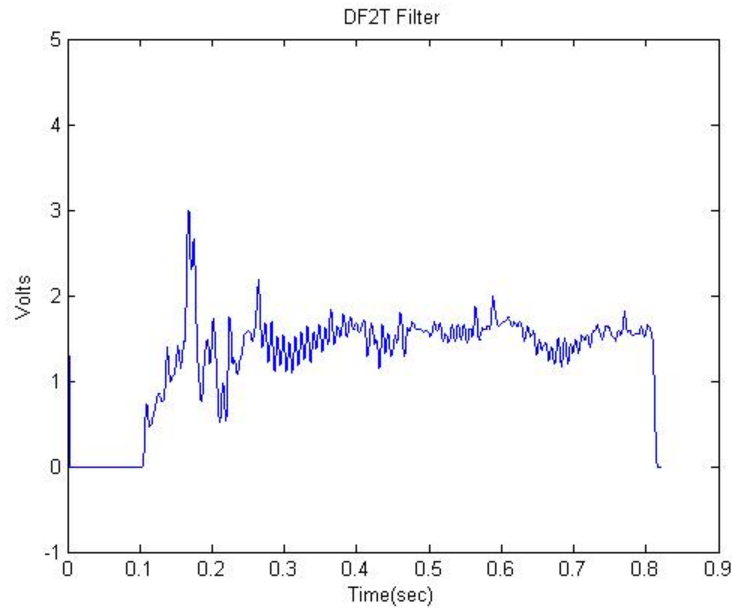


Figure 33. DF2T Filtered Signal

Upon initial inspection, a large percentage of the noise has been filtered out. But during the calculation of the currents, the DF2T filter still did not filter out enough noise to keep error calculations low. This will be discussed further later.

The second and better choice for a filter consisted of a combination of Butterworth and DF2T filters. A Butterworth filter is another commonly used filter for both analog and digital signals. In this case, the Butterworth is a digital low-pass filter.

The magnitude of the normalized transfer function is

$$|H(i\omega)| = \frac{1}{\sqrt{1 + \left(\frac{\omega}{\omega_c}\right)^{2n}}}$$

where ω_c is the cut-off frequency where the response experiences a 3-dB drop off. The order of the Butterworth filter is characterized by the parameter, n , and determines the size of the transition band or “sharpness” of the drop off. The higher order Butterworth filters do not experience much ripple in the stopband as other filters can.

The cut-off frequency, f_c , was determined qualitatively by studying the output of various filters. A balance must exist between filtering the noise and filtering important components of the signal. The following figure exhibits the output of filters with 250, 100, and 50 Hz cut-off frequencies.

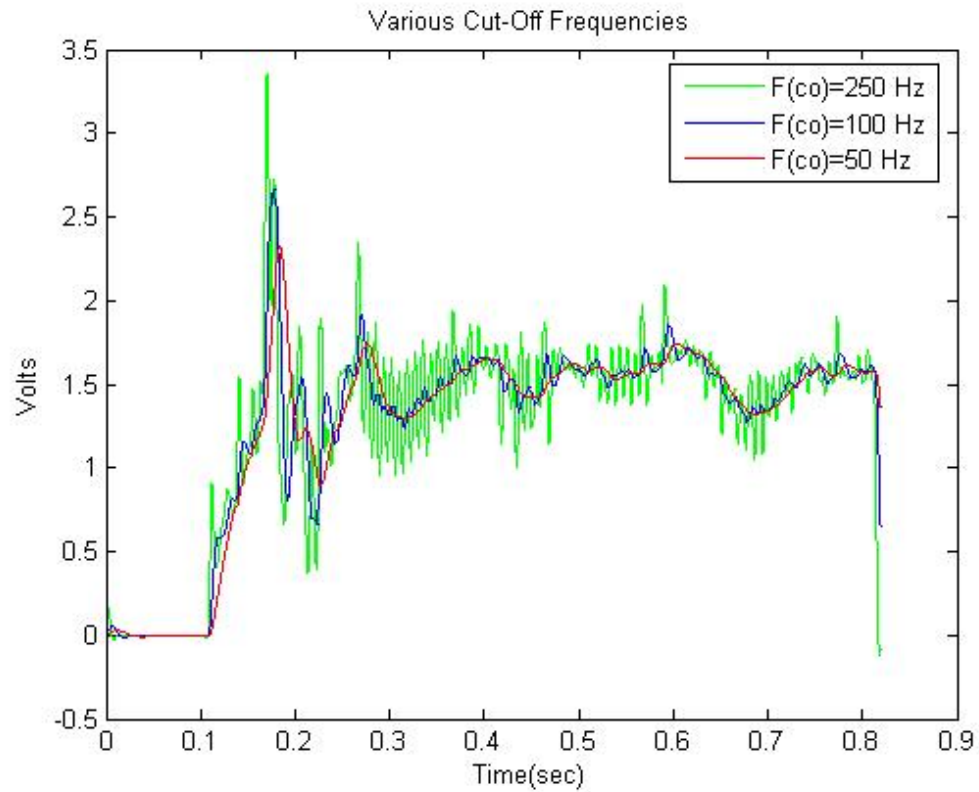


Figure 34. Filters With Various Cut-Off Frequencies

The output of the $f_{co}=50$ Hz filter best represents the signal without filtering out crucial components. This may not be readily apparent from inspection, but the error calculations discussed later will quantify the improvement.

Order (n) is the second adjustable parameter of a Butterworth filter. As mentioned earlier, the ripple is mitigated by the higher the order. In this case, very little signal difference was noticed between a third and fifth-order filter. The calculation times were also similar. The following is a comparison between a second, third, and fifth-order Butterworth filter all with a cut-off frequency of 50 Hz. The figure has been zoomed in to discern the different signals, so the original waveform is no longer recognizable. Note the slight phase shift associated with the fifth-order filter.

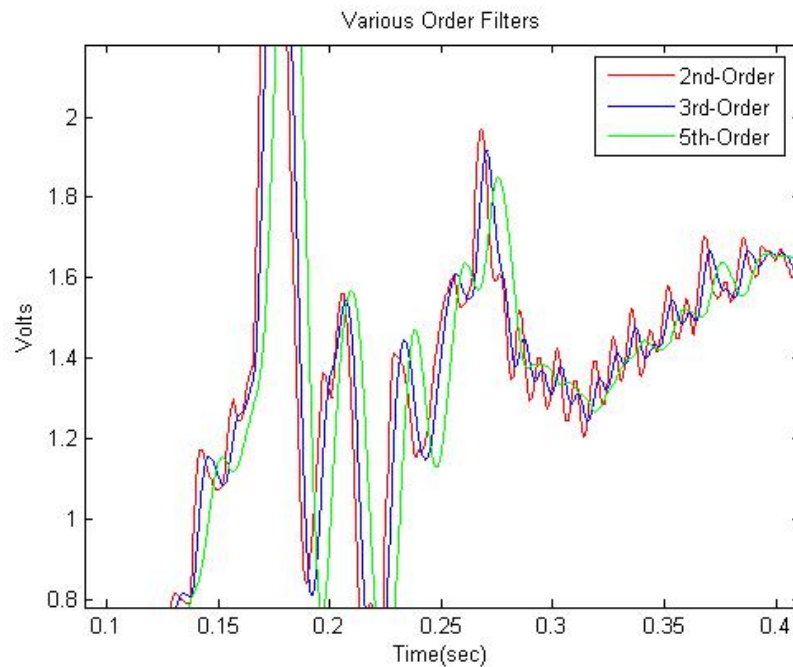


Figure 35. Filters With Various Orders

Overall, it was determined that for this data the best digital filter consists of a third-order Butterworth filter with a cut-off frequency of 50 Hz. The third order filter is a compromise between removing addition noise (better than the second-order) and inducing less phase shift (as seen by the fifth-order filter). The phase shift, or lag, may

not affect the experiment, but in an effort to reduce unknowns, a phase shift is not acceptable. The remainder of the results section will discuss data extracted through this filter.

2. Current Density Calculations

The filtered voltage signal is divided by the sensing resistor value to determine current. The current is then divided by the collector area (0.3478 cm^2) to determine current density. The collector positions are determined by measuring the gap between the two external brass fittings. Depending upon which port is in use, one of the two following formulas will calculate the position of the inner collector (collector #1) from the exhaust centerline.

$$\text{Port 1: } R(\text{cm}) = x - 5.62$$

$$\text{Port 2: } R(\text{cm}) = 4.87 + x$$

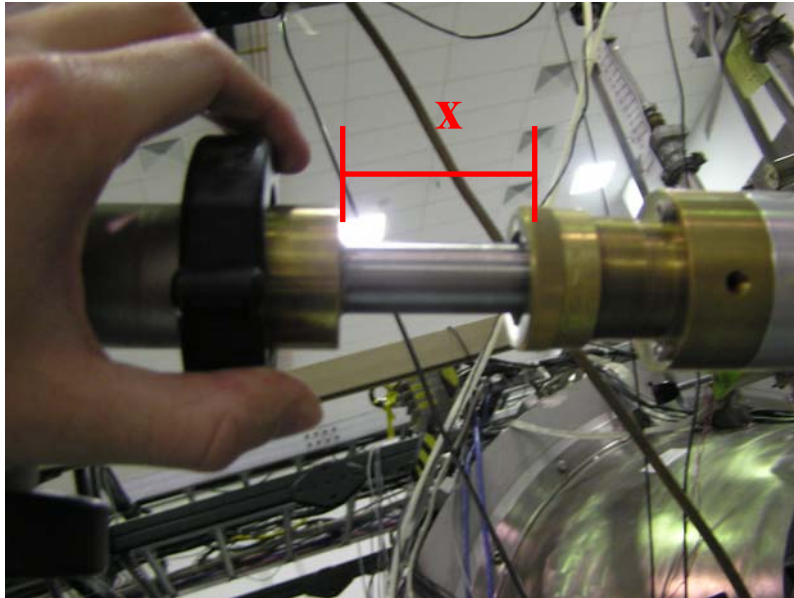


Figure 36. External Distance Measure

Unfortunately, the radial size of the plume was such that the probe could not traverse the center of the exhaust in port #2. For this reason, port #1 was used more frequently than port #2. For three days and over 150 shots, the probe was tested at various locations in the exhaust plume. The following figures show a sampling of data and describe the radial current density as a function of time for representative cases.

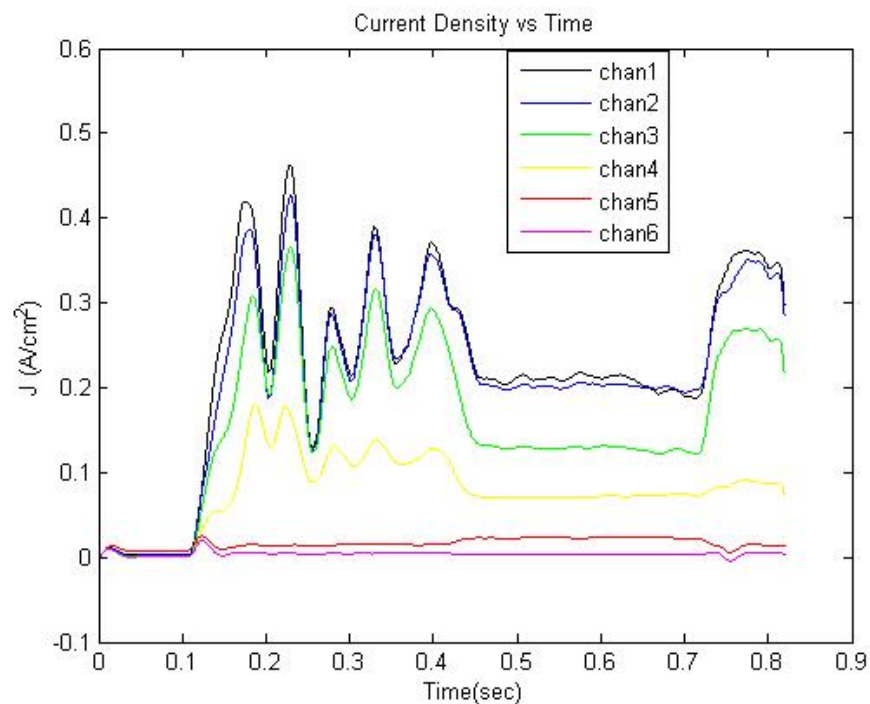


Figure 37. Port #1 Current Density Vs Time (shot 44)

Figure 37 shows a shot (data collection run) where the channel one collector was located on the far side of the plume center by 1.25 cm. This places the second collector on the other side of centerline displaced 1.75 cm.

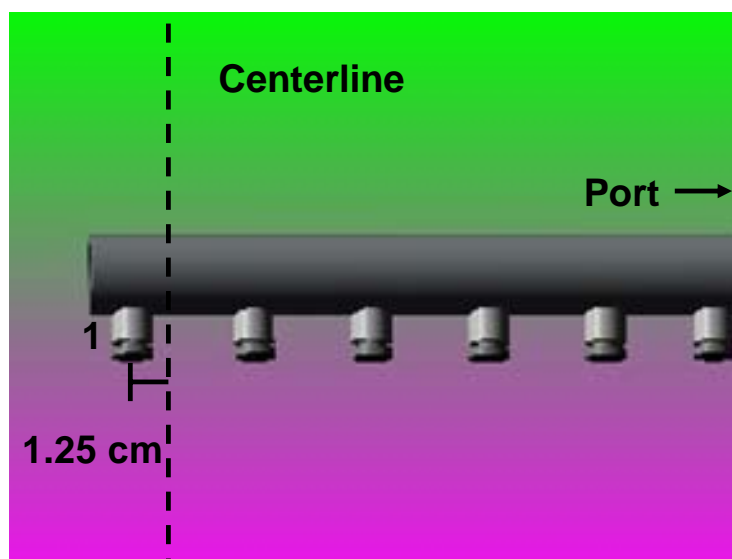


Figure 38. Position With Respect to Plasma Centerline (shot 44)

The starting plasma transients (.1-.25 sec) show current densities as high as $0.47 \frac{A}{cm^2}$ 1.25 cm from the center. The plasma current density oscillates around $0.30 \frac{A}{cm^2}$ close to center just prior to ICRH initiation (0.25-0.43 sec). Once the ICRH antenna is energized (0.43 sec), the current density ceases its oscillation and drops 30% to $0.20 \frac{A}{cm^2}$. These oscillations are an unstable characteristic of the plasma that occur under certain conditions of magnetic field, helicon power, and gas flow. The ICRH energy adds more power to the plasma and stabilizes it. The phenomenon requires additional investigation²⁹. At the end of the ICRH antenna activation (0.72 sec), the centerline current density increases 22 % to $0.32 \frac{A}{cm^2}$. The plume edge is somewhere between collectors five and six. This is evident with the fact that the current density drops to zero between collectors five and six. The plume radius is between 10.75 and 13.75 cm. By relocating the probe in the exhaust plume, the edge can be more clearly defined.

In this next example, Figures 39 and 40, collector one is now 5.6 cm from centerline. This places collector three nearest the center of the plume (0.4 cm away).

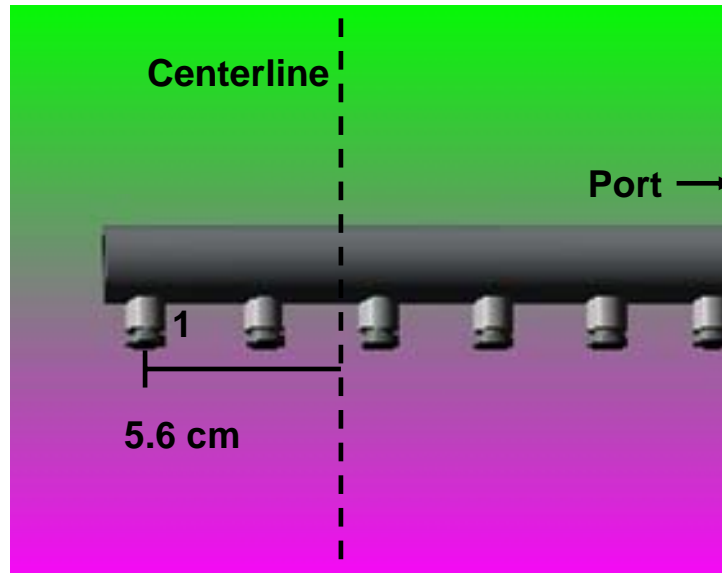


Figure 39. Position With Respect to Plasma Centerline (shot 32)

²⁹ Private Communication with Dr. Tim Glover.

The symmetry of channels one and five, two and four, confirm that the probe is positioned with collector three near the center.

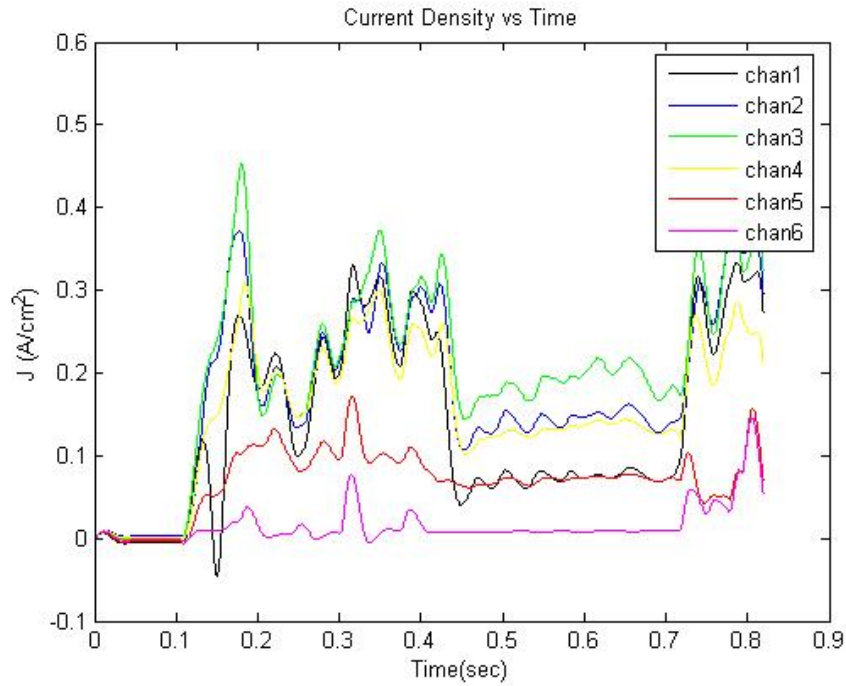


Figure 40. Port #1 Current Density Vs Time (shot 32)

Assuming that collector three is relatively close to centerline where maximum current density occurs, the previously mentioned numbers all hold true. This assumption was checked against another 12 shots that had similar configurations. The edge of the plasma is somewhere between collectors five and six (6.4 to 9.4 cm from centerline). This does not agree with the data from the previous probe position. The probe was moved again to put collector one near the center of the exhaust. The following shows the output.

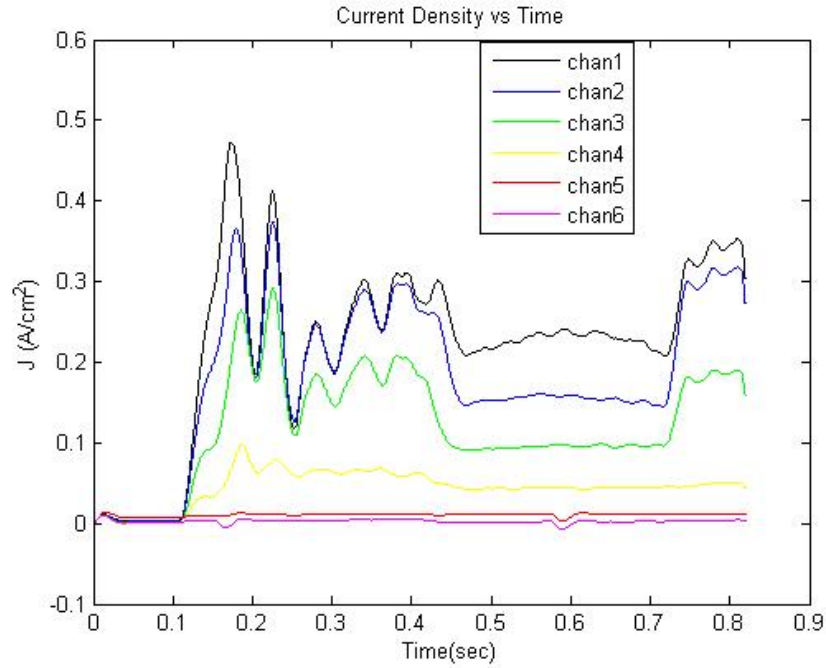


Figure 41. Port #1 Current Density Vs Time (shot 45)

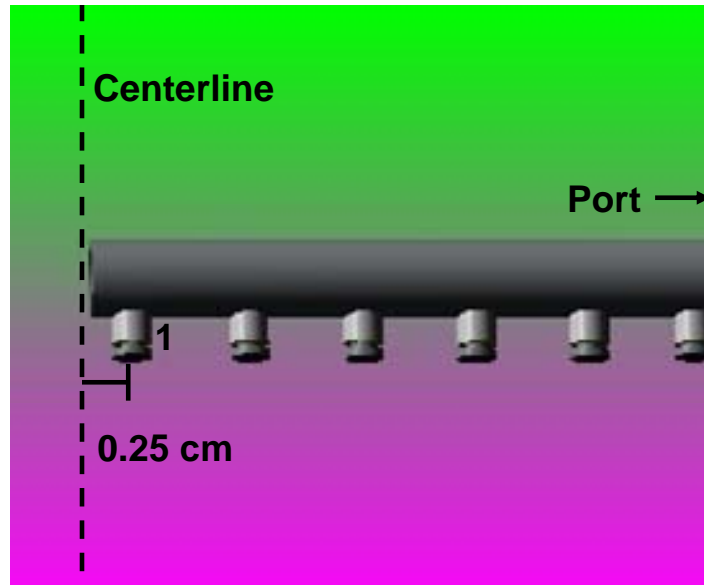


Figure 42. Position With Respect to Plasma Centerline (shot 45)

With collector one near the center of the exhaust (within 0.25 cm) the current density during initial start-up peaks at $0.47 \frac{A}{cm^2}$, then oscillates around $0.27 \frac{A}{cm^2}$. After ICRH

activation, the current density decreases 18% to an average of $0.22 \frac{A}{cm^2}$. During this period, the density peaks at $0.24 \frac{A}{cm^2}$. After ICRH is de-energized, the density rises a dramatic 46% to a peak value of $0.35 \frac{A}{cm^2}$. The edge of the plume is found between collectors four and five (9.25 and 12.25 cm from the center). Given the three positions of the probe and the corresponding plasma edge measurements, the plasma edge is somewhere between 9 and 10 cm from centerline.

The probe was then moved downstream from port #1 to port #2 and a similar analysis was conducted. At port #2, collector one never got closer than 4.87 cm to the center of the exhaust. The signal was too weak for interpretation, so the sensing resistors were moved up to 100Ω from their previous 10Ω values. The following is a typical probe reading from port #2.

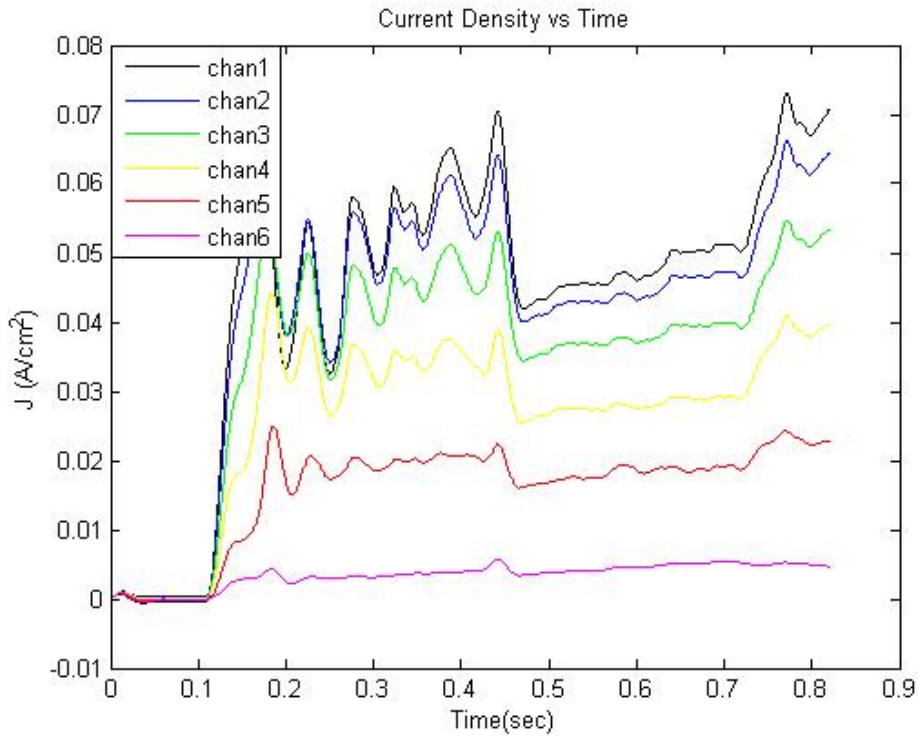


Figure 43. Port #2 Current Density vs Time (shot 42)

Prior to ICRH activation, the plasma current density has transient peaks as high as $0.070 \frac{A}{cm^2}$. Once the ICRH is energized, at approximately 0.43 sec, the current density drops 34% to an average value of $0.046 \frac{A}{cm^2}$. Similar to the results from port #1, once the ICRH is turned off, the current density jumps 58% to a peak of $0.073 \frac{A}{cm^2}$ with an average of $0.068 \frac{A}{cm^2}$. The edge of the plume in this case is close to collector six or approximately 21 cm from the center. This makes sense since port #2 is downstream of port #1 and the plume expands as it travels downstream. Shot 80, Figure 44, shows corroborating results.

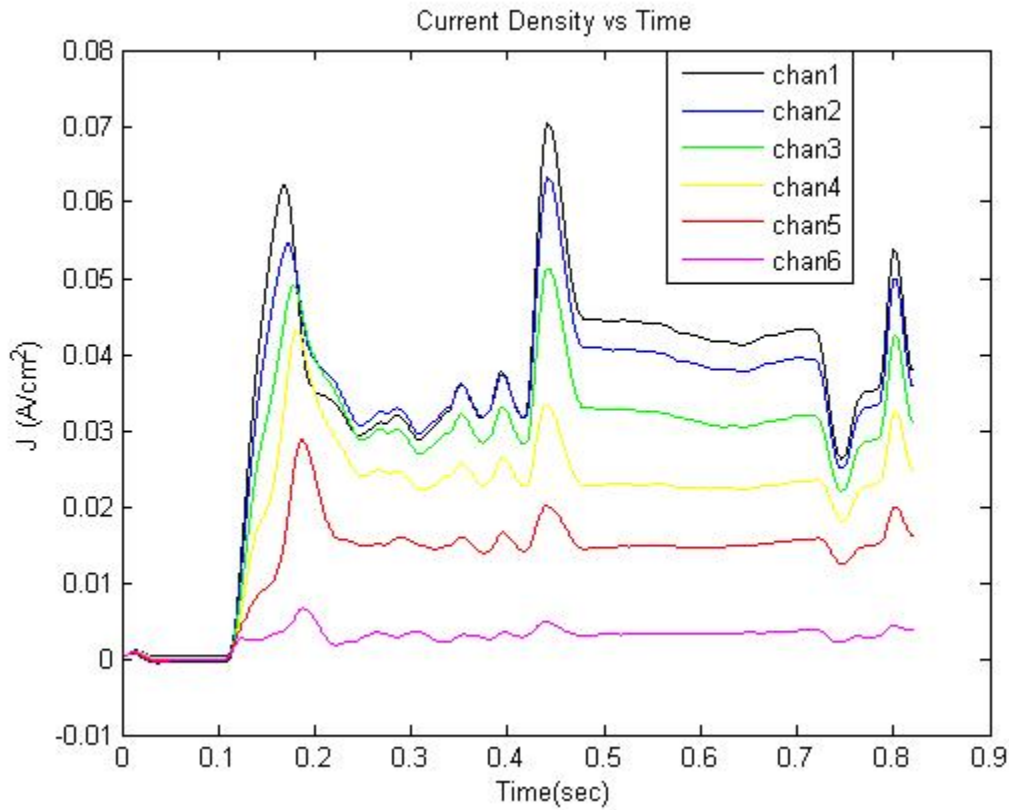


Figure 44. Port #2 Current Density Vs Time (shot 80)

This shot has an initial peak of only $0.063 \frac{A}{cm^2}$, a second peak of $0.072 \frac{A}{cm^2}$, and an ICRH-on value of $0.045 \frac{A}{cm^2}$, and but displays the same trends. The current density actually increases with ICRH on collectors one and two. The current density remains about the same both with and without ICRH for the remaining collectors. The oscillations of current density prior to ICRH activation are a result of the unstable plasma behavior that is generated with certain combinations of helicon power, gas flow, and magnetic field. This phenomenon requires more exploration and will be under investigation at ASPL in the future. Below is a picture of the actual probe immersed in a deuterium plasma.



Figure 45. Probe Immersed in Plasma

3. Current Density Radial Profile

The next step in analysis consisted of finding the average current density across the shot when the ICRH antenna is energized (ICRH window) and plotting it as a radial profile.

The current density in the ICRH window is more indicative of normal engine operations as the ICRH will be energized at all times (to varying degrees) in the operational engine. The start-up and shut-down transients were not taken into account when calculating the average current density. By eliminating these transients, the standard deviation and calculation error were minimal. The average current density was determined from 0.43 to 0.70 secs (ICRH window). The standard deviation is the square root of the bias-corrected variance

$$\sigma_{current} = \sqrt{\frac{1}{N-1} \sum_{i=1}^N (X - x_i)^2}$$

where X is the average value, x_i is the specific data point, and N is the total number of data points. A second source of uncertainty is the collector area. In this experiment, the thin sheath assumption is applicable, but this does not completely remove collector area variation. A good estimate of error is 1% of the total collector area ($\sigma_{area} = .01 * area$). This is based on the measuring accuracy of the laboratory tools. Since both causes of uncertainty in current density and collector area are indeterminate, simply adding the two numbers results in an overestimate of the total uncertainty. A better estimate of the total uncertainty resulting from independent uncertainties comes from adding the uncertainties in quadrature.

$$\sigma_{TOTAL} = \sqrt{\sigma_{area}^2 + \sigma_{current}^2}$$

The error bars in the following graphs come from adding the two uncertainties in quadrature. For Figure 46, collector one was placed approximately 1.25cm beyond the center of the exhaust.

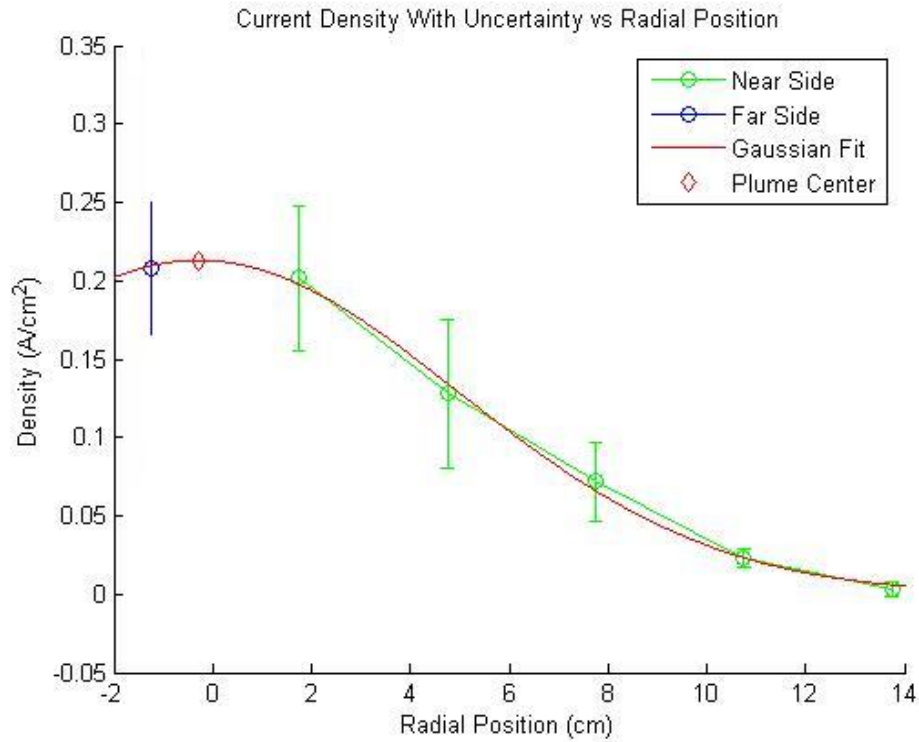


Figure 46. Port #1 Radial Profile (shot44)

The current density radial profile is definitely represented well by a Gaussian distribution. The maximum current density (at centerline) is approximately $0.21 \frac{A}{cm^2}$. The average density at collector one, $0.20 \frac{A}{cm^2}$, fits exactly with what was previously reported. The edge of the plume is somewhere between 10.5 and 14 cm (close to earlier port #1 predictions).

In Figure 47, collector one was placed 5.6 cm beyond centerline.

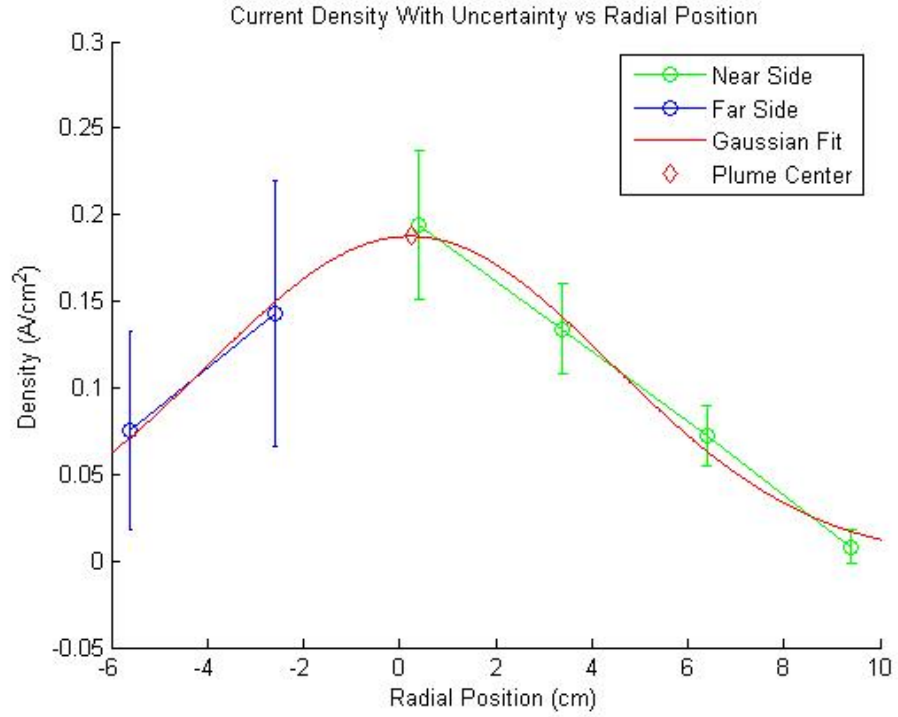


Figure 47. Port #1 Radial Profile (shot 32)

The maximum magnitude of the current density is $0.19 \frac{A}{cm^2}$. Once again, a Gaussian distribution fits the data well. The larger error at collector one (76%) and two (54%) on the negative (or far) side of centerline are caused by the large oscillations of current density within the ICRH window. The probe was next moved to place collector one at the approximate centerline of the thrust. Figure 48 shows the results.

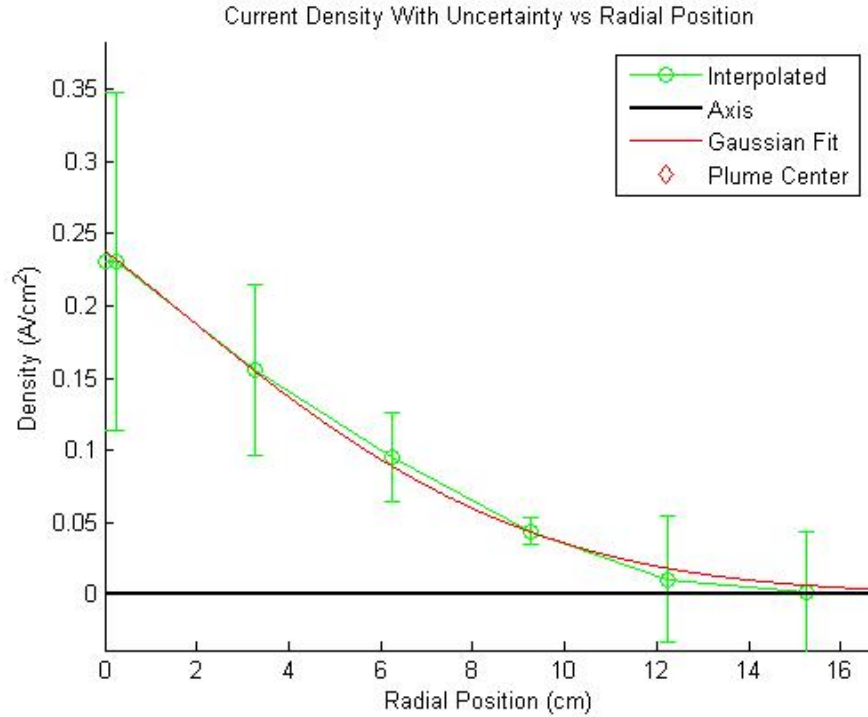


Figure 48. Port #1 Radial Profile (shot 45)

Despite the large error (50%) at collector one, the maximum average current density was $0.24 \frac{A}{cm^2}$. This large error can be attributed to the fluctuations of current density during ICRH activation as noted in Figure 41. Twelve similar profiles were studied, all with maximum current density values ranging from 0.19 - $0.24 \frac{A}{cm^2}$. In every nominal case, the radial profile is well defined by the standard Gaussian distribution. The next step was to move the probe to port #2 to investigate the radial profile further aft of the fourth magnet.

The probe was moved to port #2 and collector one was moved as close as possible to the center of the plume, 4.87 cm away. Figure 49 shows this data.

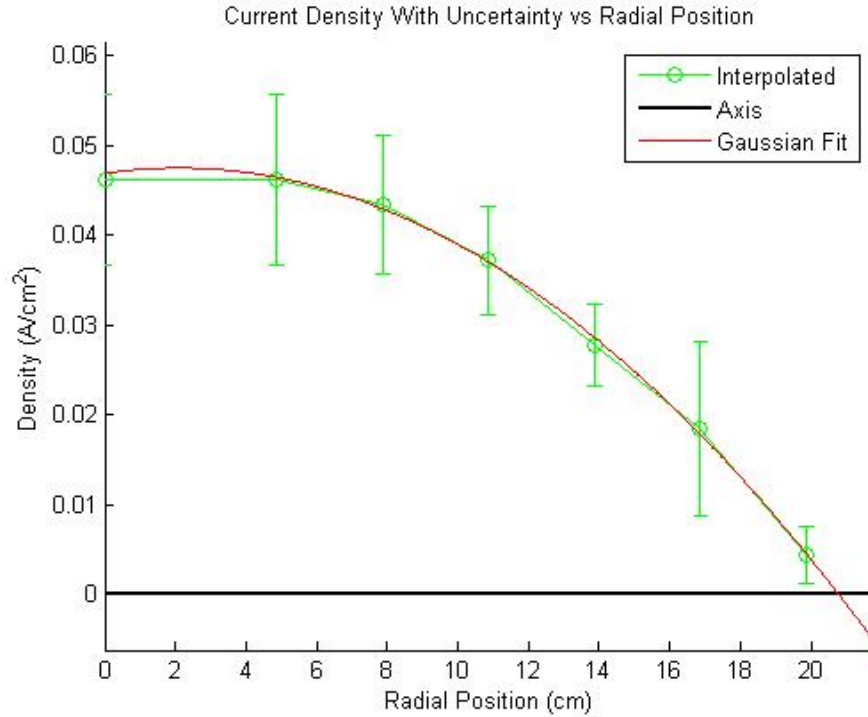


Figure 49. Port #2 Radial Profile (shot 42)

Unfortunately, the limit of the algorithm will not accurately predict the center current density. Using another MATLAB curve fitting algorithm, by forcing a Gaussian fit and setting the slope to zero at $x = 0$ cm, the predicted center current density is $0.487 \frac{A}{cm^2}$. This concurs with predictions from the temporal graphs of current density. The current density value for collector one (at $x = 4.87$ cm) is projected onto the vertical axis to facilitate reading the value. The next shot, Figure 50, shows similar results. The center current density value is extrapolated at $0.495 \frac{A}{cm^2}$. This value is within 2 % of the previous value. Several other shots agreed to within 5% of the centerline value of $.487 \frac{A}{cm^2}$.

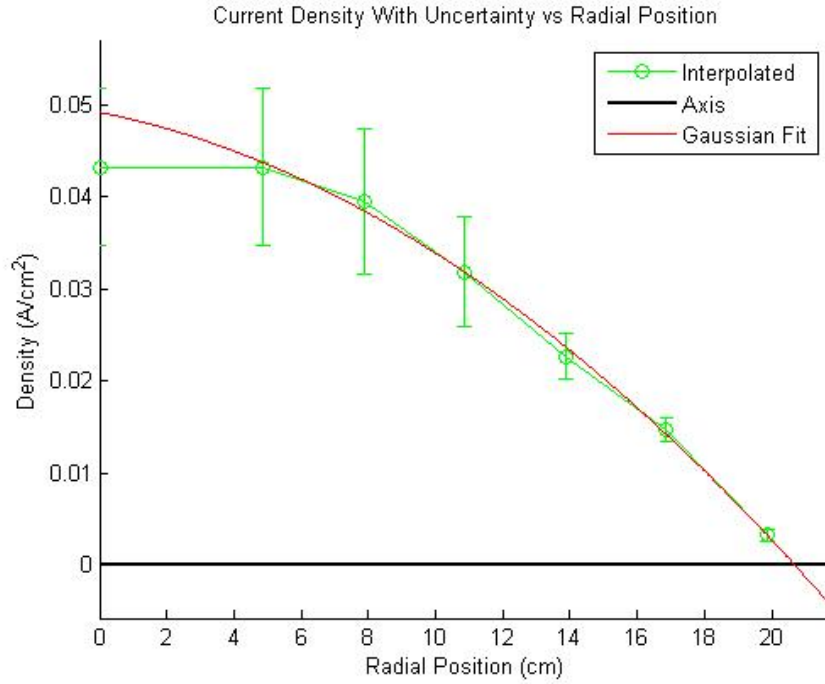


Figure 50. Port #2 Radial Profile (shot 80)

The error in both shots 42 and 80 are greatest on collectors one and two. This error is due to the fluctuations of the plasma in the ICRH window. The closer to the middle, the greater the fluctuations and the greater the error in the average current density.

Shot	Collector	1	2	3	4	5	6
42	% Error	38.67	23.67	21.08	19.20	12.60	10.90
80	% Error	48.48	48.72	22.70	22.03	32.89	72.73

Table 6. Percent Error For Shots 42 and 80

4. Flux Calculations

In addition to the current density, the particle flux is another useful parameter in determining thrust of the engine. As the ion is approximately 1800 times heavier than the electron, this experiment is more concerned with finding the ion flux of the engine. The equation to find flux (particles/cm²) from current is

$$\Gamma = \frac{I_{ion}}{e^+}$$

where e^+ is merely the charge of a single ion, 1.6×10^{-19} C. The ion current, I_{ion} , comes from the probe ion saturation current. Unlike current density, the flux requires the entire plume to be taken into consideration. To translate the one-dimensional results of the probe into the requisite two dimensions for plume cross-section analysis, annular integration is used. The annular current formula is the integral of a surface of revolution formed by sweeping the straight line between collectors around the centerline of the engine.

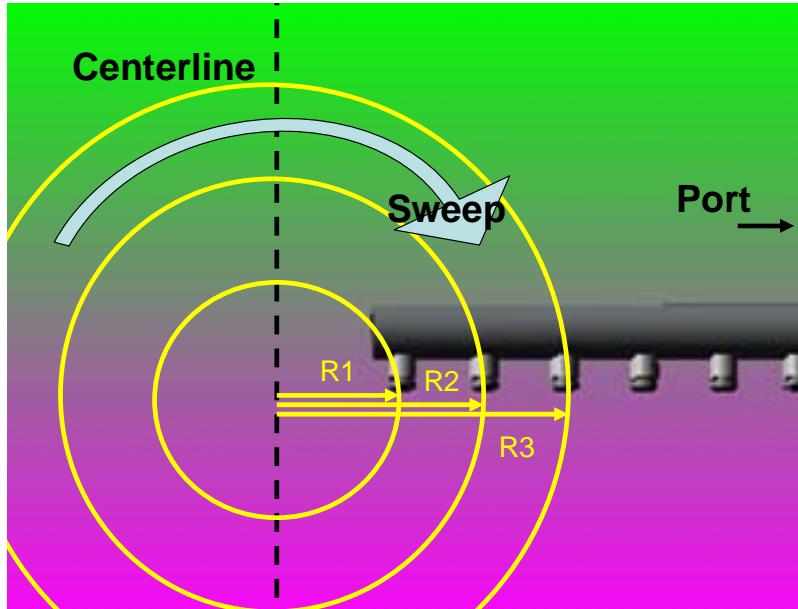


Figure 51. Annular Current Formula Calculation

The formula for finding annular current is

$$I_{ion} = \sum_{i=1}^N j_i * \pi(R_2^2 - R_1^2)$$

where the six collectors (N) will sweep out six separate annuli, each with its own current density (j_i) and inner and outer radii. For simplicity, the current density value of the annular area is the same as the collector that determines the outside radius of the annulus. Each radius is measured from the plume center to each respective collector plate. The uncertainty in current density (as previously mentioned) and error in measurement (R) were added in quadrature to assess the overall error of the calculations. The length

measurement error was considered only 1% of the actual measured values. Once again, this is based on the instruments used to measure the distances between the collectors. The following graphs show flux calculations for various shots. The integration interval is 0.001 seconds. This will help to mitigate averaging error as groups of 10 points are used to calculate every flux point. Each group of 10 is only 0.1% of the total number of data points (8192). This algorithm accounts for the fact that the probe can be anywhere throughout the plume. Collector one can be on the same side or different side from the other collectors. It starts the revolution integral at the current density peak and continues until the current density asymptotically approaches zero.

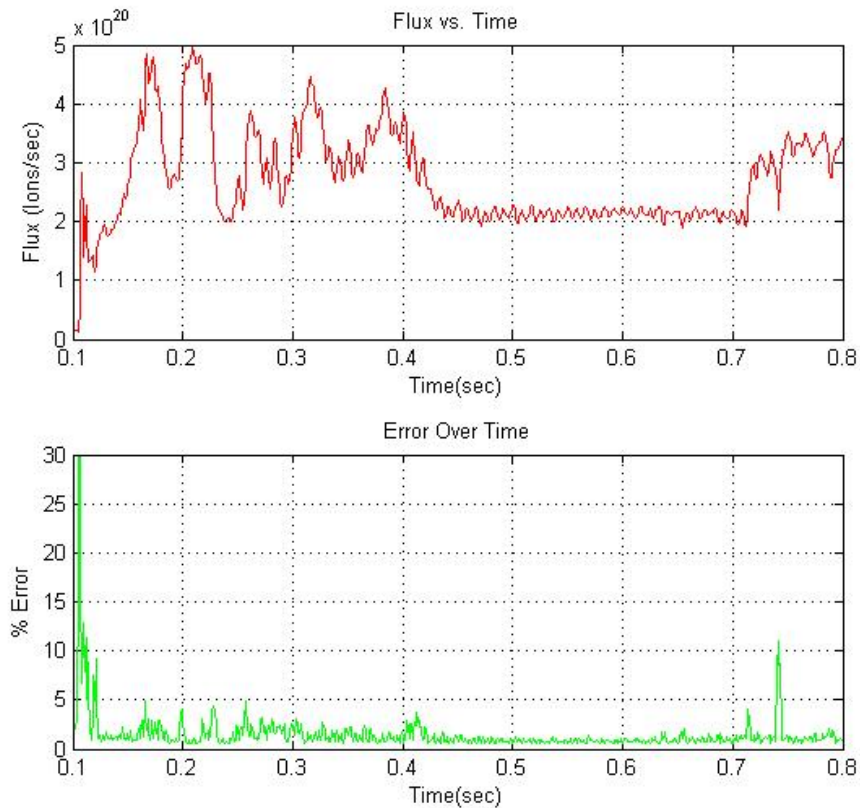


Figure 52. Port #1 Flux and Error Calculations (shot 44)

In shot 44, collector one was 1.25 cm from center on the far side of centerline. The ICRH antenna activation (0.43- 0.7 secs) produces a relatively stable ion flux at

2×10^{20} particles/sec. The standard error for this region is approximately two percent. The initial transients reach almost double this value at 5×10^{20} particles/sec, but the corresponding error with current density transients peaks at 31%. As the bulk velocity decreases (ICRH deactivation) the flux increases again to a maximum value of 3.4×10^{20} particles/sec.

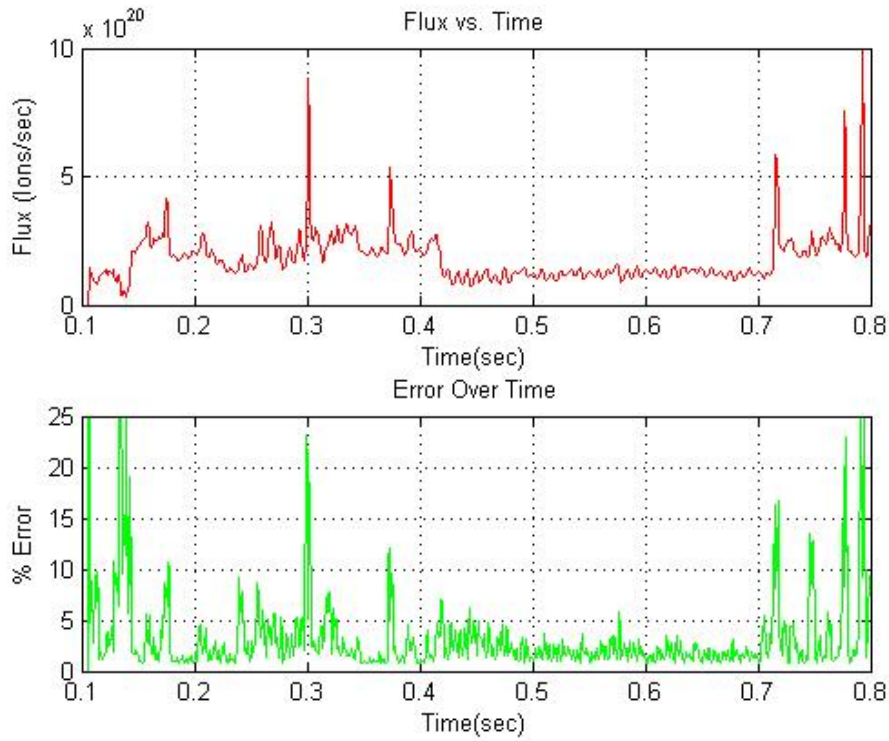


Figure 53. Port #1 Flux and Error Calculations (shot 32)

In shot 32, collectors one and two were 5.6 and 2.6 cm from centerline on the far side. Once again, the ICRH window exemplifies a stable flux of approximately 2×10^{20} particles/sec. The average error in this window is 2%.

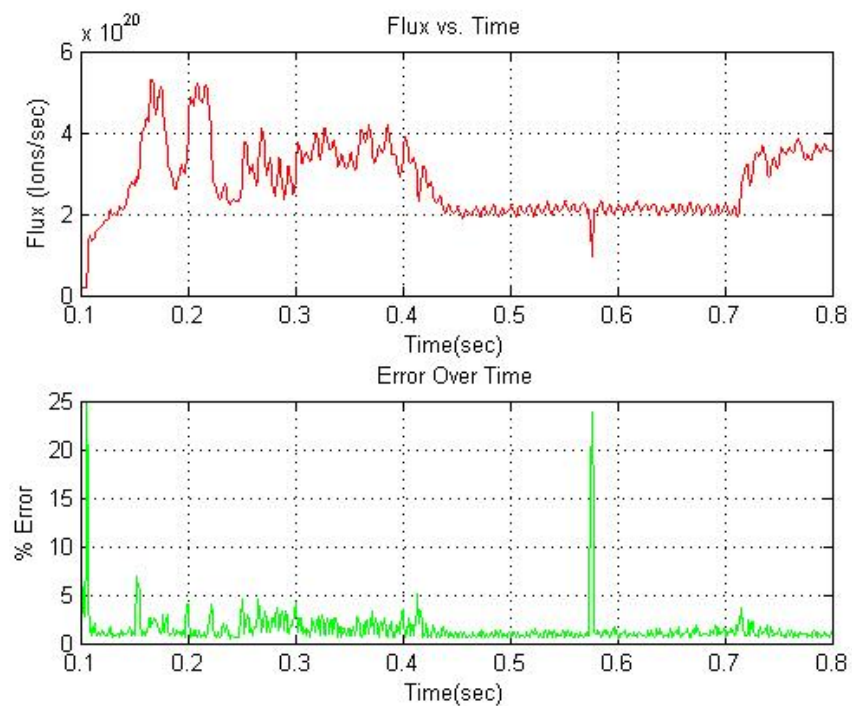


Figure 54. Port #1 Flux and Error Calculations (shot 45)

In shot 45, collector one was 0.25 cm from centerline on the near side. The flux during the ICRH window again is roughly 2×10^{20} particles/sec. The average error for this window is 2 %. The large error spike at $t = .57$ seconds is attributed to the dramatic drop in flux which, in turn, is directly related to the oscillating current density values at that same time interval.

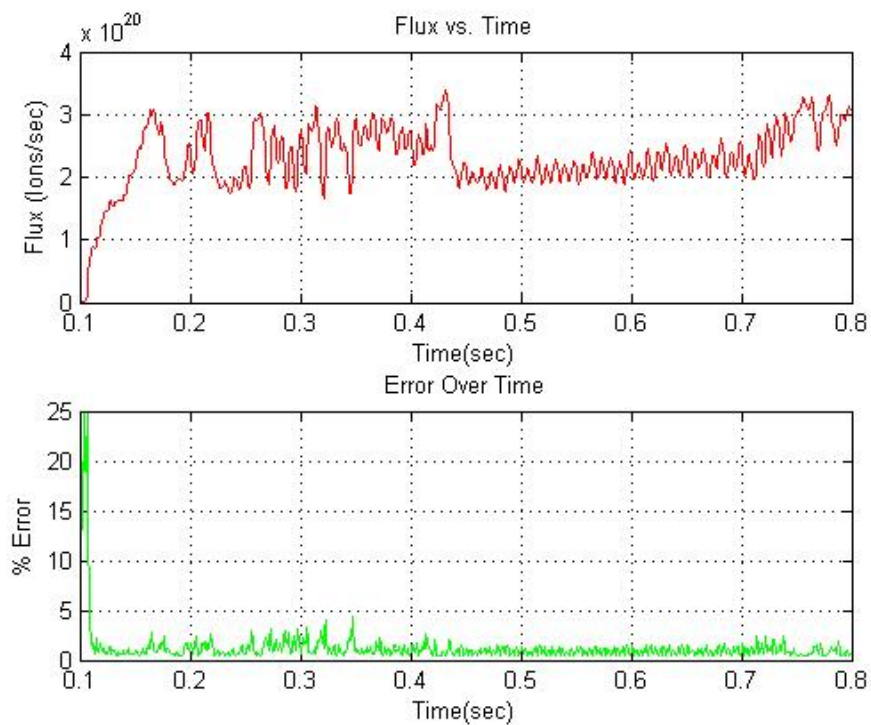


Figure 55. Port #2 Flux and Error Calculations (shot 42)

For shot 42, the probe was moved to port #2 and collector one is 4.87 cm from centerline on the near side. In the ICRH window, the flux shows a slow increase from 2×10^{20} to 2.2×10^{20} particles/sec. This slight rise of 10% can be neglected and the flux can be considered constant at 2×10^{20} particles/sec. The calculation error is hovering around 2 % the entire time.

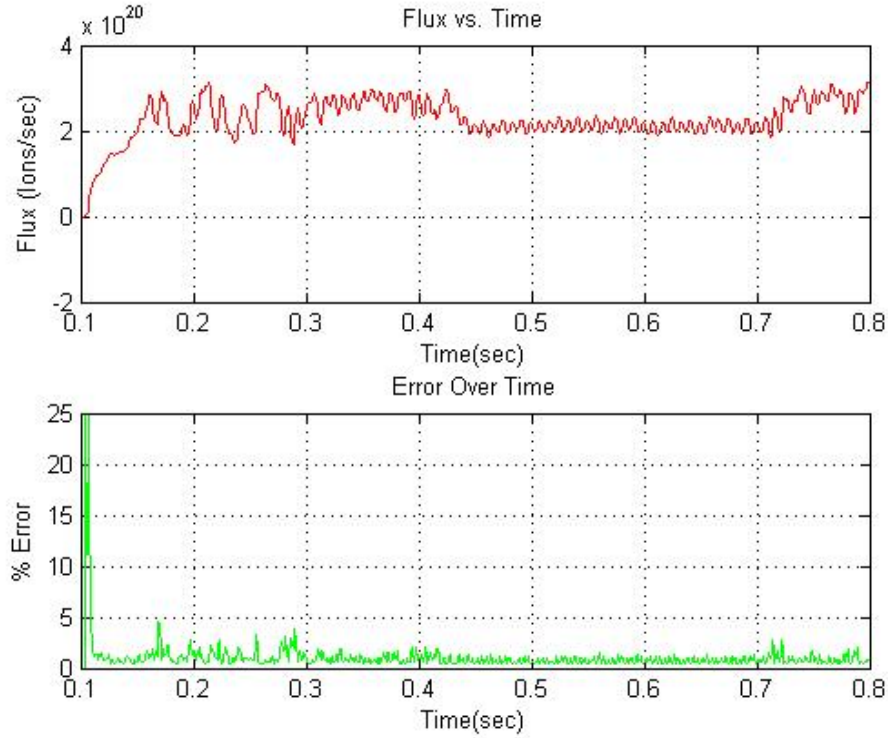


Figure 56. Port #2 Flux and Error Calculations (shot 33)

For shot 33, the collector one is 4.87 cm from centerline. The flux in the ICRH window remains relatively constant at 2×10^{20} particles/sec. The error in this window also maintains a 2 % value.

5. Ionization Efficiency

To determine the ionization efficiency of VASIMR, one must know the number of neutral gas particles entering the engine and compare that to the number of ions in the exhaust. The efficiency is defined by the ratio of output to input. The input of source gas particles is recorded for each shot. The DAQ records the count as a voltage. Using the conversion of 1 V = 200 sccm and the following equation, the source flow can be determined in terms of particles/ second.

$$\frac{\text{part}}{\text{sec}} = (\text{sccm}) * (1.80 \times 10^{-4} \frac{\text{g}}{\text{cm}^3}) * (\frac{1 \text{mol}}{2.01355 \text{g}}) * (6.022 \times 10^{23} \frac{\text{atoms}}{\text{mol}}) * (\frac{1 \text{min}}{60 \text{sec}})$$

Where 1.80×10^{-4} is the density of Deuterium under standard temperature and pressure. The atomic weight of Deuterium is 2.01355 AMU. Avogadro's number and the

conversion of minutes to seconds complete the conversion. Below is the graph of gas flow for shot 44 and is indicative of all shots previously discussed.

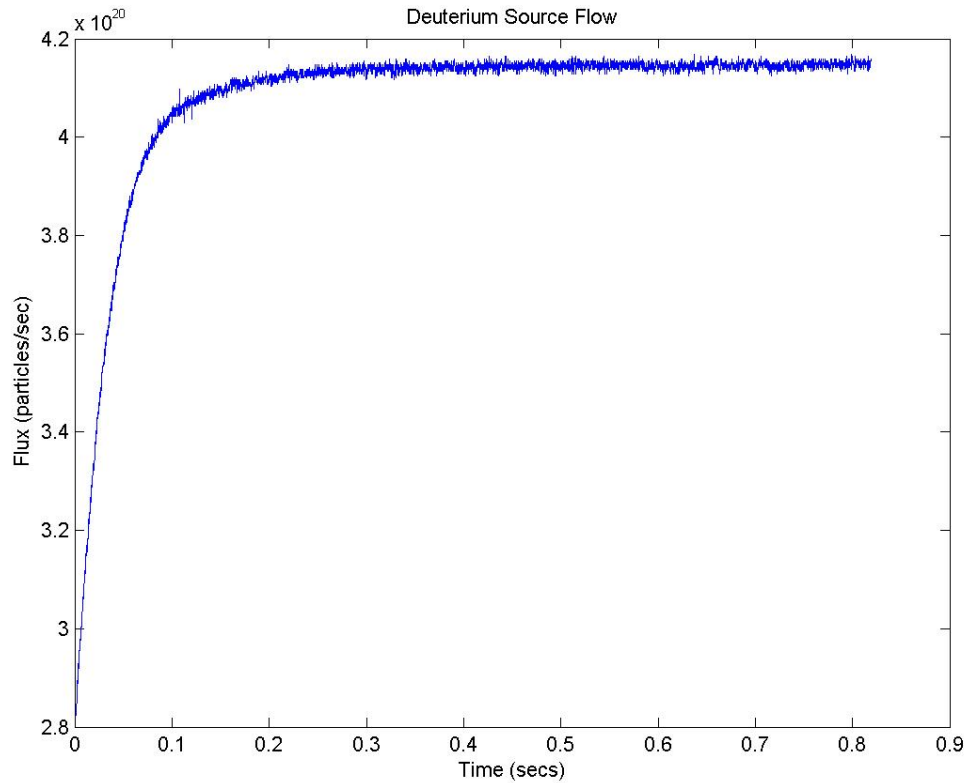


Figure 57. Standard VASIMR Gas Flow for Deuterium

Given the average flux from probe ($2 \times 10^{20} \frac{\text{ions}}{\text{sec}}$) and the average source flux of $4.1 \times 10^{20} \frac{\text{particles}}{\text{sec}}$, the ionization efficiency is 49%. This number conforms with other ASPL ionization estimates. The ionization efficiency is expected to dramatically increase with additional power to both the ICRH and Helicon antennas.

6. Field Line Dragging Experimental Results

The results of the probe were most dramatic when placed in port #2. Both of current polarity radial profiles are dramatically different from the exhaust with no coil current (shot 80). In the following graph, shot 58 had a forward coil current of 70A. Shot 94 had a reverse coil current of 70 A.

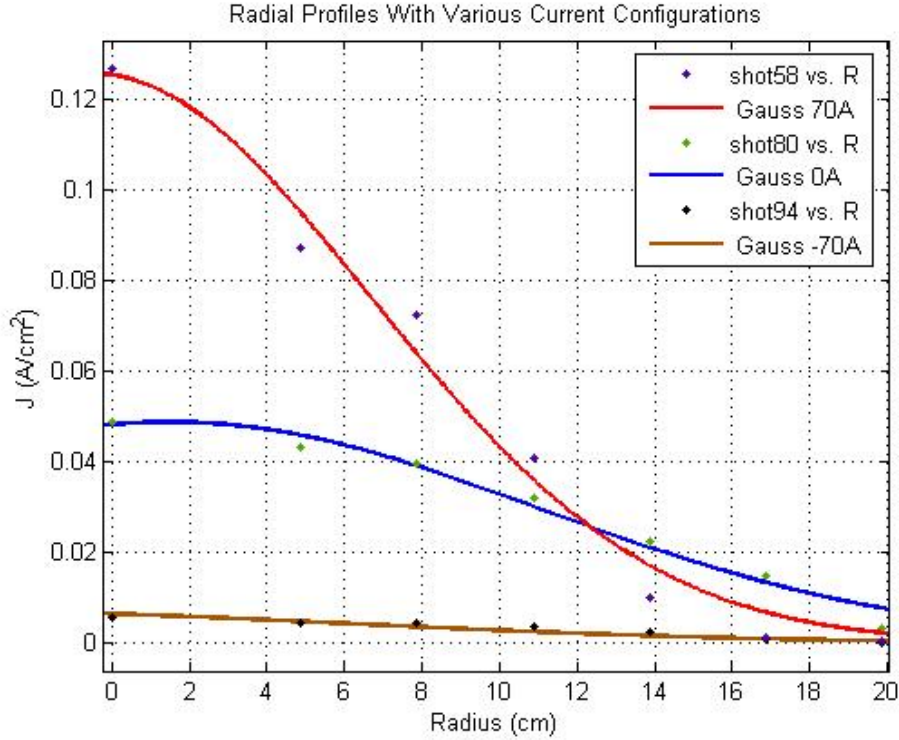


Figure 58. Radial Profiles with Varying Coil Currents

As indicated by Figure 57, the forward polarity coil current (shot 58) created a weak magnetic region in the exhaust. The peak current density jumped almost 165% ($0.127 \frac{A}{cm^2}$) from a nominal $0.048 \frac{A}{cm^2}$. The super-Alfvénic plasma dragged the field lines of the engine into the exhaust and produced a tightly collimated exhaust signature. When the coil current was reversed (shot 94), a strong reverse field was created. This strong field actually opposed the flow of plasma and dramatically reduced the peak current density of entire plume from $0.048 \frac{A}{cm^2}$ to $0.007 \frac{A}{cm^2}$ (a drop of 85%).

THIS PAGE INTENTIONALLY LEFT BLANK

IV. CONCLUSIONS

A. RADIAL PROFILE VERIFICATION

All the results showed that the radial profile of the plasma at both ports conforms to a Gaussian distribution. The large deviations from the average current density values (error bars) are due to the oscillatory nature of the plasma. This maybe due to an unstable plasma potential before application of ICRH power. This unstable characteristic is still under investigation by ASPL. The error could be further reduced by greater precision in the construction of another probe. The Gaussian fit of the profile helps to validate some ASPL mathematical models of VASIMR as well helping to validate the field line dragging experiment.

B. FIELD LINE DRAGGING EXPERIMENT

ASPL's experimental predictions were substantiated by the probe's readings with full forward current of 70 A and full reverse-bias current of 70 A. The results of this experiment need to be calibrated with the Faraday cup that was in place at the time of experimentation, but the relative magnitudes of each current density are dramatically different enough to illustrate the plasma's different reactions to the varying magnetic fields. In the future, this probe may help to determine exactly where the plasma exhaust detaches from the magnetic field lines -- producing thrust. It may also be used to explore ways to optimize exit nozzle geometry.

C. FLUX AND IONIZATION EFFICIENCY

The annular integration method to flux determination uses some simplifications that proved to be acceptable. The largest simplification is the assumption that the current density across the entire annulus is exactly what is measured at the outside radius collector plate. Due to the oscillatory nature of the plasma, the flux was only calculated during its more stable moments during the shot (in the ICRH window). The resultant flux calculations, when compared to ASPL models, were in agreement. The ionization efficiency of 50% agreed with ASPL predictions given certain power, gas flow, and magnetic field conditions. Full ionization is only achievable with a certain combination

of magnetic field strength, ratio of helicon field to peak field, gas flow rate, and power.³⁰ These tunable parameters are similar to tuning the combustion parameters (mixture, temperature, pressure) to achieve optimal jet engine output. ASPL expects the efficiency to increase dramatically with additional total power input and after further investigation into optimizing the tunable parameters of VASIMR.

³⁰ Private Conversation with Dr. Tim Glover.

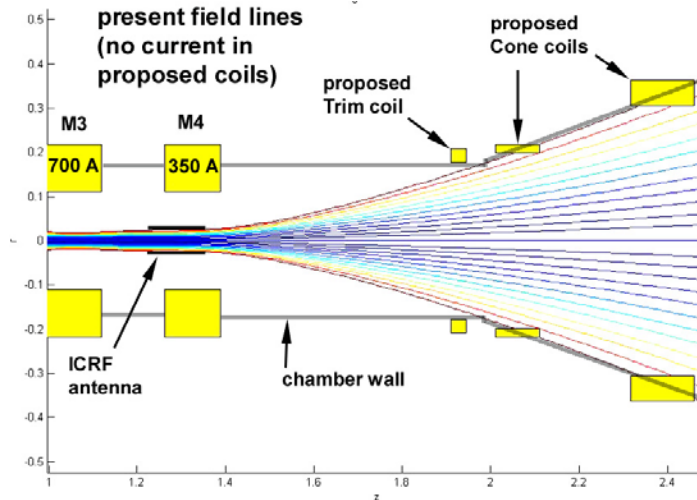
APPENDIX A. A PROPOSED DEMONSTRATION OF FIELD-LINE DRAGGING IN VASIMR

Tim Glover

revised Dec. 20, 2004

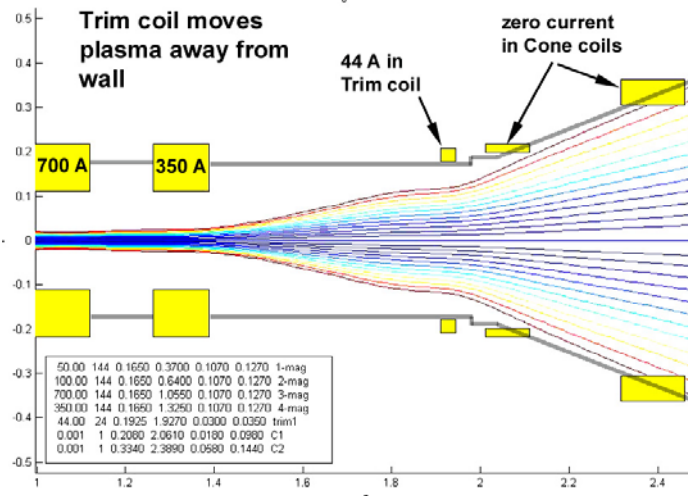
Objective: to demonstrate that when super-Alfvénic plasma flow enters a region of weak magnetic field, the embedded field is dragged into the weak field region.

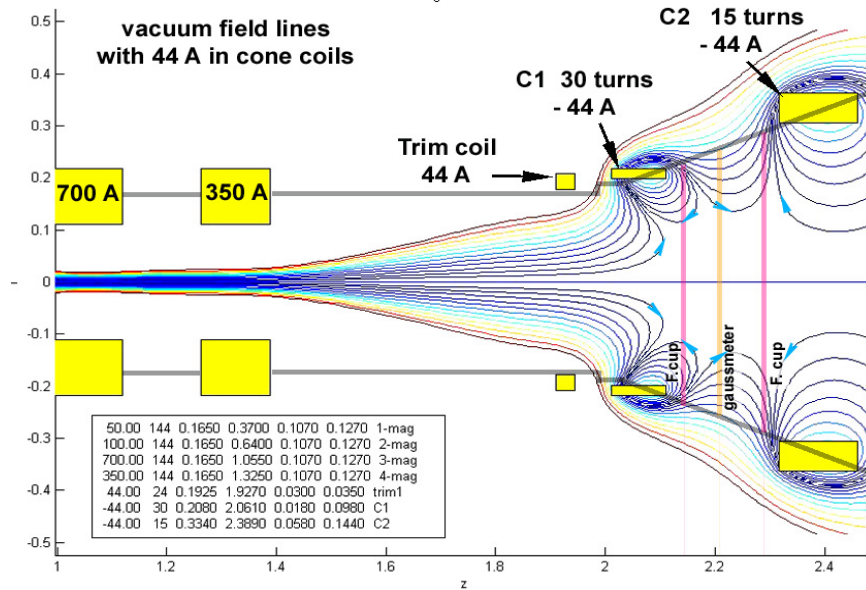
Strategy: by adding a number of coils to the conical section of the ASPL vacuum chamber, the relatively weak field of the four VASIMR magnets in the exhaust plume can be made nearly zero, or reversed to form a cusp. By also adding a trim coil, the plasma can be pushed off the chamber walls. The field lines near the axis of the machine remain nearly straight, roughly approximating the conditions in Boris' nozzle model. We should see some dragging of the field lines with the 20 kW helicon plasma, compared to the vacuum field. Addition of ICRH power should further drag the field lines, relative to those for the helicon alone.



In the figure at left, I have plotted the field lines for our typical deuterium discharge. The field lines are spaced 2 mm apart at the exit of the ICRF antenna. The vacuum field lines indicate that the plasma edge intersects the upstream edge of the cone. The locations of the proposed Cone coils are dictated by the space available among the 10" ports, QF40 ports and lifting point welded onto the cone.

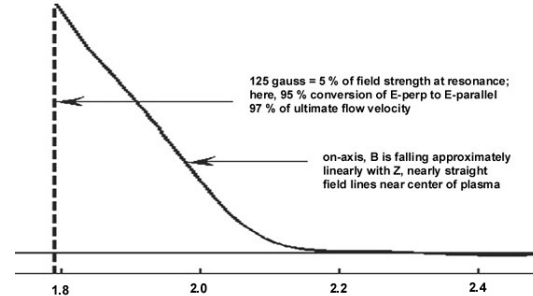
The figure at right shows how the trim coil pushes the plasma away from the chamber walls. The field strength here is approximately 100 gauss, so virtually all of the conversion of perpendicular ion energy to parallel has taken place, relative to the ICRF resonance field.





The figure above displays the field lines for a set of coils that produces a large volume of weak *vacuum* field (less than 5 gauss on-axis). Also shown are the radial lines accessible to our gaussmeter and Faraday cup. The gaussmeter is mounted on top of the chamber on a QF40 port, while the Faraday cup is mounted on the side of the chamber, on either of two QF50 ports spaced 15 cm apart.

The figure at right indicates the on-axis field strength. This shows that for the plasma near the axis, the super-Alfvénic transition takes place in a region of nearly straight field lines. This central core will therefore be both detached and *highly directed* as it enters the high-beta/weak field volume, and should drag the nearly axial field lines with it into the region where the vacuum field would be much weaker if field-line dragging did not occur.



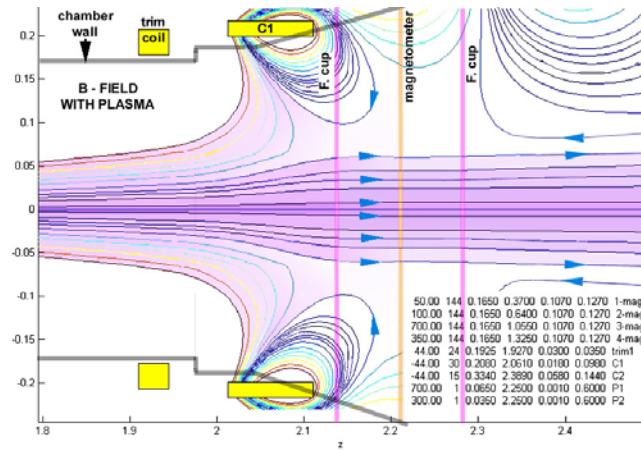
The plasma density profile is typically peaked at the center, so that the kinetic energy density drops off with increasing radial position in the plasma. This means that beta, the ratio of kinetic energy density to magnetic energy density, is also a decreasing function of radial position. Therefore, what I expect to see is the tenuous outermost plasma following the vacuum field lines, the central core of dense plasma dragging higher field strength downstream, and some transition between the two cases at intermediate radial positions. When ICRF is applied, the kinetic energy density is multiplied several times, so that at any particular axial position, the super-Alfvénic transition should move outward in radius. The core of detached plasma should acquire a larger radius and be more tightly collimated, since the super-Alfvénic transition will also move upstream, where the field lines are more nearly parallel to the axis.

Diagnostic capabilities:

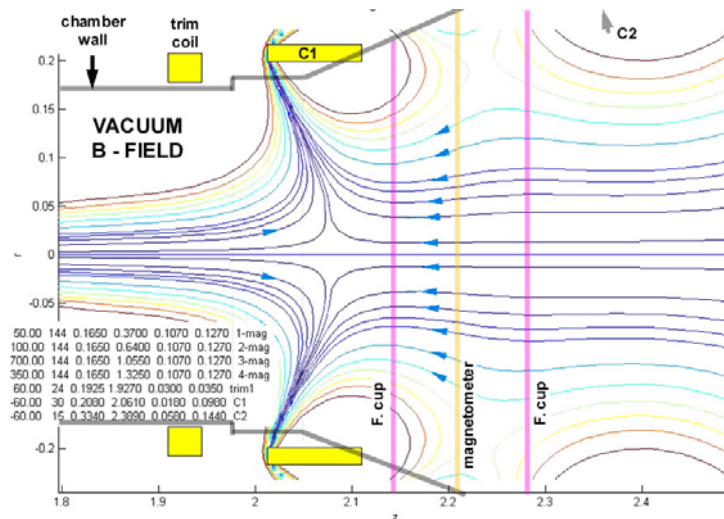
- The gaussmeter has a precision of 1 milligauss, bandwidth of 10 kHz, and can measure B_z , B_r , and B_θ , though not simultaneously. In a single plasma shot, one of these quantities can be obtained at a single radial location as a function of time.
- The Faraday cup measures ion flux with a spatial resolution of 1 cm as a function of time. Like the gaussmeter, it remains fixed during a shot so we obtain data at only one radial location per shot.
- With Brian Sinclair (Naval Postgraduate School), I am building a linear array of Langmuir probes. This will be a single alumina shaft with 10 tantalum collectors. Each will be 1/4 inch (6 mm) in diameter, spaced approximately one inch apart. With these probes biased to collect ion saturation current, we will have the radial shape of the exhaust plume as a function of time, with a bandwidth of 50 kHz.
- The thrust target is restricted to measurements along the axis of the experiment but can move from a point near the downstream side of magnet 4 (350 A) to a point roughly two meters away, well past the downstream end of the cone.
- Alfonso has built a Rogowski coil (approximately 2 cm in diameter), which we might use to search for azimuthal currents.

Expected Results:

I expect that *some* portion of the plasma near the axis will reach super-Alfvénic flow before the field lines begin diverging into the cusp. This plasma should drag its nearly axial field lines into the low field volume. The gaussmeter should indicate different radial profiles of the axial, radial, and possibly azimuthal field components. The Faraday cup should show more total flux, with the flux concentrated near the axis. The linear array of Langmuir probes under construction by Brian Sinclair for his master's thesis should give us radial profiles of ion current as a function of time, whose amplitudes can be calibrated by the Faraday cup. Power and gas scans should show these effects increasing with plasma density. If 10 kW of ICRF power is available, scanning ICRF power should show even more dramatic effects. Below is a speculative picture of the anticipated difference from the vacuum field. Even very small effects should be discernible with the diagnostics we have available.

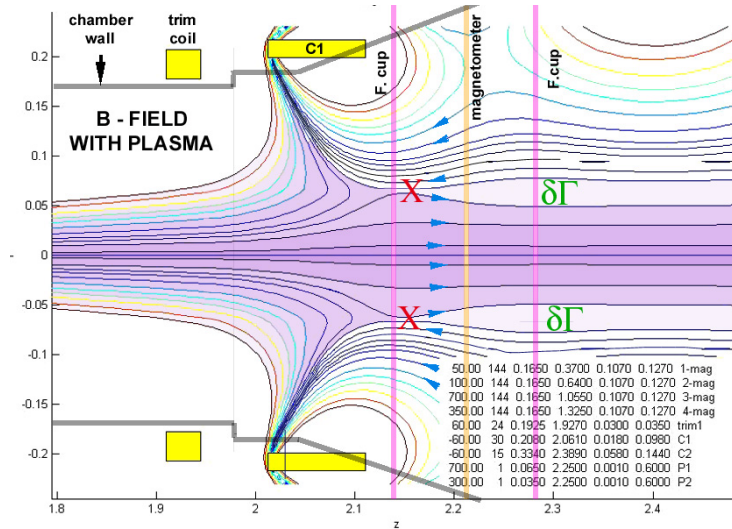


If the field line-dragging is minimal, a stronger cusp may produce more distinct effects. The vacuum field for this case is shown below. Rather than a volume of near-zero field for the diagnostics to scan through, we have a volume of reversed (vacuum) field. I have in mind a field strength of 10 – 20 gauss along the gaussmeter's scan line, so that the Earth's field makes only a minor contribution.



For this case, the gaussmeter (labeled 'magnetometer' here) should show a reversal of the sign of the axial field component when the helicon is turned on, if there is line dragging. A radial scan may show the field pointing upstream outside of the plasma, and pointing downstream inside the plasma. The Faraday cup and linear Langmuir probe array can indicate clearly which field lines bear plasma and which do not.

The figure below indicates another phenomenon to search for in this reversed field case:



At the points marked with a red 'X', reconnection seems certain. If so, as the gaussmeter/magnetometer moves radially inward, I expect that we would first see the upstream-pointing vacuum field, then a region of fluctuating field at the plasma edge, then the downstream-pointing field of the plasma core. For a radial scan of the Faraday cup moving inward along its downstream scan line, I would expect little or no plasma along the upstream-pointing field lines, then fluctuations (indicated by the green ' $\delta\Gamma$ ') in ion current propagating downstream from the reconnection region, then a much stronger ion current as the cup enters the downstream-pointing field region. I would expect the turbulent reconnection region and the plasma edge to occur at larger radii as the density and ICRF power are increased. Time-resolved reconnection events may or may not be observable due to the limited bandwidth of the diagnostics. The gaussmeter will not be able to resolve fluctuations in field above 10 kHz, the Langmuir probe array will be limited to 50 kHz, and the Faraday cup is limited to 100 kHz.

Apparatus: We have one power supply that can deliver 70 A at up to 20 V. We have approximately 400 feet of 8 AWG cable, and approximately 100 feet of 2/0 cable. I'm trying to track down a higher-current power supply for the Trim coil. In short, I think we have what we need to produce the desired fields.

THIS PAGE INTENTIONALLY LEFT BLANK

APPENDIX B. MATLAB TEMPORAL CURRENT DENSITY PROGRAM

```
function[fresult] = LPfilter(path,date,shot,Resvec,X1,t1,t2)
%
% LPfilter extracts, filters (noise above 50 Hz), and plots current
% density
% from the 6-collector linear flux probe. It then finds total current
% and
% uncertainty by calling the m-file IsatIntegral.
%
% input:
%       Resvec: the vector of sensing resistances. The measured
% values of the
%               sensing resistors are used in the current
% calculation.
%
%       X1: the distance between collector 1 and the center of
% the
%           plasma; sets the radial positions of the remaining
%           collectors. A negative value of X1 indicates that
% the
%           probe has been pushed across the center of the
% plasma.
%
%           This is expected to be the usual case, since taking
%           data across most of the plasma profile allows us to
%           better ascertain the location of the center of the
%           profile.
%
%       t1: beginning of the time interval over which the
% collector
%           currents are measured for the flux calculation.
%
%       t2: end of the time interval over which the collector
%           currents are measured for the flux calculation.
%
% sample call: LPfilter('C:\LParray\','2005-03-
% 25',44,Resvec,3.0,0.5,0.7)

collpos = [0.0:3.0:27.0]; % rel pos'ns of the (0.262" dia.)
collectors
R1 = collpos(1:6) + X1; % vector of collector pos'ns rel
centerline
NC = 6; % number of collectors active
delR1 = 0.005*2.54*ones(1,NC); % uncertainty in relative collector
positions
%-----
----
%Creating the 3rd-order low-pass butterworth filter
%f(cutoff)=50Hz,f(sample)=10000
[q,v] = butter(3,50/10000);
Hd = dfilt.df2t(q,v); %Direct-form II transposed structure
```

```

%-----
----
% Retrieve the raw data, filter, and store in 'LPdata'
LPdata = zeros(NC,8192);
for i = 1:NC;
    is = num2str(i); % the channel number as a string
    chan = strcat('LParrrayC',is); % append the channel number to
                                % form the complete channel name.
    shotdata = get_data_T(path,date,shot,chan);
    LPdata(i,:) = shotdata.data/(.3478*Resvec(i));%collector area .3478
cm^2
    LPdata(i,:) = filter(Hd,LPdata(i,:));%implement filter
end
%-----
----
% Timing data
info = get_shot(path,date,shot);
rate = info.rate(5);
Ndata = 1.0/rate;
tgen = 0.0; % start time for general diagnostics, including pressure
gauges
time = Ndata*[1:1:8192] + tgen;
% convert the start and stop times to data byte numbers:
n1 = round((t1 - tgen)*rate);
n2 = round((t2 - tgen)*rate);
Npts = n2 - n1 + 1; % number of data points for use in calculating
the average
                                % and standard deviation of the current of each
                                % collector

%-----
----
%Finding average J and deviation
Iavg = zeros(1,NC);
delI = zeros(1,NC);
for i = 1:NC;
    Iavg(i) = sum(LPdata(i,n1:n2))/Npts;
end
var = zeros(1,NC);
for i = 1:NC;
    for j = n1:n2;
        var(i) = var(i) + (Iavg(i) - LPdata(i,j))^2;
    end
end
stddev = (var/(sqrt(Npts-1))).^0.5;
Iavg,stddev
%-----
----
%Plotting the results
plot(time,LPdata(1,:), 'k')
hold on;
plot(time,LPdata(2,:), 'b')
plot(time,LPdata(3,:), 'g')
plot(time,LPdata(4,:), 'y')
plot(time,LPdata(5,:), 'r')
plot(time,LPdata(6,:), 'm')

```

```

title('Current Density vs Time');
xlabel('Time(sec)');
ylabel('J (A/cm^2)');
legend('chan1','chan2','chan3','chan4','chan5','chan6');
pause
close
%-----
----
%Calling another program to find current profile with uncertainty
Isatintegral2(R1,delR1,Iavg,stddev)

```

THIS PAGE INTENTIONALLY LEFT BLANK

APPENDIX C. MATLAB RADIAL PROFILE PROGRAM

```
function[] = Isatintegral(R1,delR1,I1,delI1)

% This is a program from ASPL that has been modified to accept
% data from linear Langmuir probe array. This program accepts
% data in any order and sorts by position. Multiple data points
% at a single position are averaged, with their errors combined in
quadrature.
%
% Calculates the total ion current based on measurements taken by the
% linear Langmuir probe array at different radii and uses linear
interpolation
% between the measured data points.

% Input:  R    radial positions of Langmuir Probe collectors [cm]
%         delR  uncertainty in R values [cm]
%         I     current measured by the Faraday cup [A]
%         delI  standard deviations of the individual current
measurements [A]
%-----
----
% Area of the collectors (cm^2)
radius = 0.262*2.54/2;    %nominal diameter of 0.262"
Ap = 3.14159*radius^2      %individual probe collector area
% uncertainty in the collecting area (sheath effects):
delAp = Ap*.01;    % same for all measurements here, but may be
assigned
% individual values as sheath effects become
significant
% where the plasma density drops at the plume edge.
%-----
----
% Interpolation Guide
% I = interp1(Ri,Ii,R, 'nearest');
% 'nearest' Nearest neighbor interpolation
% 'linear' Linear interpolation (default)
% 'spline' Cubic spline interpolation
% 'pchip' Piecewise cubic Hermite interpolation
%-----
----
[Rsort,ind1] = sort(R1)
'sort R:'    % sorted in order of increasing position
R = R1(ind1)
delR = delR1(ind1);
I = I1(ind1)
delI = delI1(ind1);
j=I;        % Ion current density
n = length(R);
n1 = n-1;
%-----
---
```

```

% Standard deviation of each current measurement is added in quadrature
% to each measurement's uncertainty in aperture area, to estimate
uncertainty in
% current density: (note that this algebraic form avoids division by
% small values of I)
delj = ((delI./Ap).^2 + (I.*delAp/(Ap^2)).^2).^(1/2)

% plot the unprocessed current density, with errorbars:
%errorbar(R,j,delj,'ro-')
%hold on;

if (R(1) >= 0.0)    % if the first position in the sorted position
                    % vector is positive, there is no need to switch
                    % measurements from the other side to the positive
side.
    %'flag: R(1) is positive'
    ra = R(1:n1);
    rb = R(2:n);
    ja = j(1:n1);
    jb = j(2:n);

elseif (R(1) < 0.0)
    'flag: R(1) is neg'
    % if data extends beyond the axis, the points beyond are
    % switched to the 'near' side of the axis;
    % if locations on the 'far' side have measurements at
    % corresponding locations on the near side, they are averaged with
    % the near side data, and these average values
    % are inserted as additional near side data points.
    [Rsort,ind1] = sort(R);
    'check sort'
    R(ind1)
    neg = find(Rsort < 0);
    negind = ind1(neg);
    jneg = j(negind);
    deljneg = delj(negind);
    Rneg = Rsort(neg);
    pos = find(Rsort >= 0);
    posind = ind1(pos);
    jpos = j(posind);
    deljpos = delj(pos);
    Rpos = Rsort(pos);
    %-----
    % The 'switch' quantities are the measurements from negative
    % positions, flipped over to the corresponding positive
    % positions.
    Rswitch = abs(fliplr(Rneg));
    jswitch = fliplr(jneg);
    deljswitch = fliplr(deljneg);
    % append the switched data to the positive position data and sort
    Radd = [Rpos,Rswitch];
    jadd = [jpos,jswitch];
    deljadd = [deljpos,deljswitch];
    [Raddsort,indadd] = sort(Radd);
    jaddsort = jadd(indadd);

```

```

deljaddsort = deljadd(indadd);
[fresult1]=fit(R',j','gauss1');
%-----
%Graph if some collector positions are negative
figure(1)
errorbar(Rpos,jpos,deljpos,'go-')
hold on
errorbar(Rneg,jneg,deljneg,'bo-')
plot(fresult1);
plot(fresult1.b1,fresult1.a1,'rd');
title('Current Density With Uncertainty vs Radial Position');
ylabel('Density (A/cm^2)');
xlabel('Radial Position (cm)');
legend('Near Side','Far Side','Gaussian Fit','Plume Center');
%errorbar(Rswitch,jintrp,deljswitch,'mo-')
%-----
% change the names of the switched and re-sorted data vectors back
to the
% original names to make the current calculation
R = Raddsort;
j = jaddsort;
delj = deljaddsort;
end
pause
close
%-----
% search through the data for points with identical radial
positions;
% average these together and replace with a single point; error for
% average is standard deviation of original measurements from the
% average.
nadd = length(R);
nadd1 = nadd - 1;
nadd2 = nadd - 2;
totrep = 0;
m = 1;
i = 1;
while (m <= nadd)
    m
    if (m >= nadd)
        Rred(i) = R(nadd);
        delRred(i) = delR(nadd);
        jred(i) = j(nadd);
        deljred(i) = delj(nadd);
        break
    end

    thisR = R(m)
    nextR = R(m+1)

    if (nextR == thisR)
        'flag: repeated position'

        repeats = find(R == thisR);
        repj = j(repeats);

```

```

    repdelj = delj(repeats);
    repdelR = delR(repeats);
    nrep = length(repeats);

    totrep = totrep + nrep;
    jred(i) = sum(repj)/nrep;
    deljred(i) = sqrt((1/(nrep-1))*sum((repj - jred(i)).^2));
    delRred(i) = sqrt(sum(repdelR.^2)/nrep);
    Rred(i) = thisR;
else
    jred(i) = j(m);
    deljred(i) = delj(m);
    Rred(i) = R(m);
    delRred(i) = delR(m);
end
i = i + 1;
m = i + totrep;
if (m > nadd)
    Rred(i) = R(nadd);
    delRred(i) = delR(nadd);
    jred(i) = j(nadd);
    deljred(i) = delj(nadd);
end
end
'while over'

R = Rred;
delR = delRred;
j = jred;
delj = deljred;
%-----
if (R(1) ~= 0.0) % the plasma current density is assumed uniform
                % between the axis and the first data point
    'flag: R(1) > 0'
    R = [0,R];
    xdelR = delR(1);
    delR = [xdelR,delR];
    xj = j(1);
    j = [xj,j];
    xdelj = delj(1);
    delj = [xdelj,delj];

end
% size(R);
% R
% size(I)
% I
% size(j)
% -----
% fitting a curve to the radial profile
%[fresult]=fit(R(1,2:7)',j(1,2:7)', 'gauss1');
[fresult]=fit(R(1,2:7)',j(1,2:7)', 'poly2');
%center=[fresult.b1,fresult.a1]; %identifying the peak of the curve
n = length(R);
n1 = n-1;

```

```

% plot the current density, with errorbars:
figure(2);
errorbar(R,j,delj,'go-')
hold on;
topj = max(j);
topdelj = max(delj);
jtop = 1.1*(topj + topdelj);
jbot = -0.1*jtop;
Right = 1.1*max(R);
Rleft = min(R);
if (Rleft > 0)
    Rleft = 0.0;
end
axis([Rleft Right jbot jtop])
horax = zeros(1,2);
xaxis = [Rleft, Right];
plot(xaxis,horax,'k','LineWidth',2);
hold on;
plot(fresult);
%plot(fresult.bl,fresult.al,'rd'); %red diamond signifying center of
plume
title('Current Density With Uncertainty vs Radial Position');
ylabel('Density (A/cm^2)')
xlabel('Radial Position (cm)');
legend('Interpolated','Axis','Gaussian Fit','Plume Center');
ra = R(1:n1);
rb = R(2:n);
ja = j(1:n1);
jb = j(2:n);
%-----
--
% Finding the flux
% The annular current formula is the integral of a surface of
revolution
% formed by sweeping the straight line between current density values
around
% the current axis (consider plot of current density vs radial
position):
Ii = (2*pi/3)*(jb.*(rb.^2 - rb.*ra./2 - (ra.^2)/2) - ja.*(ra.^2 -
rb.*ra./2 - (rb.^2)/2));
DR = (R(n) - R(n1))/2;
Ri = R(1:n1) + DR;

I2 = sum(Ii)
%-----
--
% uncertainty by second method
% (delj is formed earlier by combining in quadrature the standard
% deviation of the current measurement with the uncertainty in the
% collecting area.)

delra = delR(1:n1);
delrb = delR(2:n);
delja = delj(1:n1);
deljb = delj(2:n);

```

```

dIdjb = (pi/3)*(2*(rb.^2) - rb.*ra - ra.^2);
dIdja = (pi/3)*(2*(ra.^2) - rb.*ra - rb.^2);
dIdrb = (pi/3)*(jb.*(4*rb-ra) + ja.*(2*rb+ra));
dIdra = (pi/3)*(ja.*(4*ra-rb) + jb.*(2*ra+rb));

% vector of (squares of) uncertainties in the current through each
annulus
sigI2i = dIdjb.^2.*deljb.^2 + dIdja.^2.*delja.^2 + ...
        dIdrb.^2.*delrb.^2 + dIdra.^2.*delra.^2;

% uncertainty in the total current is the quadrature sum of
% the uncertainties in the individual annuli:
delI2 = sqrt(sum(sigI2i))
percent = 100*delI2/I2;
'percent error:', percent
% electronic charge:
e = 1.6E-19;
flux = I2/e

```

APPENDIX D. MATLAB FLUX DETERMINING PROGRAM

```
function[]=fluxiteration(path,date,shot,Resvec,X1,t1,t2,m)

%m=size of step interval
% Sample Call: fluxiteration('C:\LParrray\','2005-03-
29',21,Resvec,4.87,0.1,0.8,.05)
%-----
----
c=int16((t2-t1)/m);%rounds to the nearest integer
fluxvec=ones(1,c);%size vector
timevec=ones(1,c);
errorvec=ones(1,c);
for i=1:c;
    LPflux(path,date,shot,20,Resvec,X1,t1,t1+m);
    fluxvec(i)=ans;
    timevec(i)=t1;
    t1=t1+m;
end
t1=timevec(1,1);
for i=1:c;
    LPflux2(path,date,shot,20,Resvec,X1,t1,t1+m);
    errorvec(i)=ans;
    t1=t1+m;
end

gasflow(date,shot);
sccm=ans;
t=[.0001:.0001:.8192]'

subplot(2,1,1)
plot(timevec,fluxvec,'r');
hold on;
%subplot(2,1,1)
plot(t,sccm,'b');
title('Gas Flow/Flux vs. Time');
xlabel('Time(sec)');
ylabel('Flux (Ions/sec)');
grid on
subplot (2,1,2)
plot(timevec,errorvec,'g');
title('Error Over Time');
xlabel('Time(sec)');
ylabel('% Error');
grid on;
```

THIS PAGE INTENTIONALLY LEFT BLANK

APPENDIX E. MATLAB GAS FLOW PROGRAM

```
function[parts]=gasflow(date,shot)
extract=get_data_T('C:\LParray\',date,shot,'Gas Flow');
%need to work on conversion factor
%Verlin said that 1V=200 or 300 sccm, but what is conversion of
%sccm to part/sec
sccm=extract.data;
t=[.0001:.0001:.8192];
%atoms/cm^3=density(g/cm^3)*(1/Atomic Wt(AMU))*Na
%sccm*(atoms/cm^3)*(1 min/60 sec)=part/sec
dens=1.8e-4;
AMU=2.01355;
Na=6.02214e23;
conv=dens/AMU*Na/60*200;
parts=sccm*conv;
plot(t,parts)
title('Deuterium Source Flow')
xlabel('Time (secs)')
ylabel('Flux (particles/sec)')
```

THIS PAGE INTENTIONALLY LEFT BLANK

INITIAL DISTRIBUTION LIST

1. Defense Technical Information Center
Ft. Belvoir, VA
2. Dudley Knox Library
Naval Postgraduate School
Monterey, CA
3. Dr. Chiold Epp
Johnson Space Center, NASA
Houston, TX
4. Dr. Chris Brophy
Naval Postgraduate School
Monterey, CA
5. Dr. R. Panholzer
Naval Postgraduate School
Monterey, CA
6. Dr. Franklin Chang Diaz
Adastra Rocket, Sonny Carter Training Facility
Houston, TX